Ultracataclastic vein evolution within a granodiorite along the Naxos Detachment System

Olivia Rolfe

A thesis submitted in partial fulfillment of the requirements for the
Master of Science in Earth Sciences

Department of Earth and Environmental Sciences
Faculty of Science
University of Ottawa

Abstract

Ultracataclastic and pseudotachylytic veins are interpreted as direct evidence of coseismic slip, reflecting the conditions and mechanisms associated with fault rupture. Although the Naxos granodiorite, Greece, is known for its pristine pseudotachylyte exposures, these features remain largely understudied in terms of their microstructural evolution and implications for middle crust seismicity. We examine a suite of well-preserved veins hosted in the deformed Miocene granodiorite, historically described as examples of melt-origin pseudotachylytes, but here are re-interpreted as dominantly ultracataclasites, produced from the comminution of host rock. The veins occur in the immediate footwall of the fluid-rich Naxos-Paros Detachment System, active between c. 12-9 Ma, and possess a similar composition as the surrounding host rock of primarily albite (35%), quartz (25%), orthoclase (16%), and biotite (12%). Structural field observations from the highest strain zone reveal three distinct crosscutting vein sets. Electron backscatter diffraction mapping of host rock porphyroclasts of albite, orthoclase, and quartz crosscut by ultracataclastic veins demonstrates that cataclasis is the dominant deformation mechanism. Variations in microstructural maturity of vein fragments suggest episodic emplacement, with rupture exploiting pre-existing slip planes. Cuspate phase boundaries between orthoclase and albite, initially observed in optical and scanning electron microscopy, are confirmed by electron microprobe analyses as a result from dissolution-precipitation reactions. These features indicate deformation by dissolution-precipitation creep. The results suggest that fluid-mediated reactions localized at vein tips contributed to weakening, generating a mechanical-chemical feedback loop that promoted ultracataclastic vein propagation along the detachment.

Acknowledgements

This project was funded by an NSERC Discovery grant awarded to D.A. Schneider, an Ontario Graduate Scholarship and a Geological Society of America Graduate Student Research grant awarded to O. Rolfe. We would like to thank G. Poirier (University of Ottawa) for assistance with SEM and microprobe data acquisition. Thanks also to K. Onaat and C. Bakowsky (University of Ottawa) for thoughtful discussion during manuscript preparation.

Foremost, I want to thank my supervisor, David Schneider, for his time, wisdom, and continuous support over the course of my degree. He has provided me with many opportunities which have contributed significantly to my growth as a researcher. Dave's commitment to his students and his field creates an environment that is exciting, challenging, and one I feel very fortunate to have been part of.

I am grateful to Renelle Dubosq for her mentorship and enthusiasm in this project. Her patience and willingness to answer all of my questions (especially pertaining to the EBSD analysis) is deeply appreciated. I also thank her for her time spent completing the EBSD and micro-XRF data acquisition. I am very excited to continue learning under her supervision as a PhD student!

I thank Bernhard Grasemann at the University of Vienna for his expertise and insightful feedback throughout this project. I also thank Stefan Zaefferer at the Max Planck Institute for Sustainable Materials for his assistance with EBSD data acquisition and spherical indexing, which was crucial for obtaining high-quality maps and orientation values.

During my MSc, I was employed by the Geological Survey of Canada to work on a national fault inventory, and I want to thank my excellent supervisors at the GSC for their support and flexibility in enabling me to complete both projects.

I am also grateful to Dave for assembling such an excellent group of students who have made my time at uOttawa so bright. To my friends in the DAS lab: Christina, Laurence, Kaan, Taylor, Jenn, Camryn and Victoria, thank you for all the laughs, invaluable advice, coffee runs, and international exploits.

A huge thank you to my family (Mom, Dad, Cari, Tia, Alex, Nico, Pablo, Lucia, Aba, Rachel) for always cheering me on! I especially thank my mom, whose determination and perseverance has been a constant source of motivation. I am also grateful to my partner, Ethan, for his steadfast encouragement and patience over the past two years, which have been instrumental to my success.

Lastly, I owe a special thanks to Djordje Grujic and Anne-Marie Ryan at Dalhousie University for fostering my interest in earth science and preparing me for my graduate studies.

Table of contents

1. Introduction

Earthquake rupture processes control the distribution of strain, promote fluid migration, and govern the evolution of fault zone architecture in the crust. Structural investigations of fault zones (e.g., Heermance et al., 2003; Barth et al., 2013) and experimental studies on frictional behavior (Mair & Marone, 1999; Brantut et al., 2008) have documented that slip during a rupture event localizes along principal rupture surfaces that accommodate the majority of deformation within a fault core (Segall & Pollard, 1983; Platt et al., 2015). Rupture propagation involves the breakdown of the host rock by cracking at the rupture tip (process zone), which scales with the dimension of the slipping patch (Swanson, 1992; Cowie & Shipton, 1998). Earthquake ruptures proceed at slip rates on the order of meters per second (Scholz, 2019), and numerical simulations have illustrated that strain localization intensifies with increasing rupture speed (Barras & Brantut, 2025). Earthquake ruptures will preferentially propagate along pre-existing zones of weakness, such as joints, fractures, or previous slip surfaces (Segall & Pollard, 1983; Chester & Chester, 1998; Chester et al., 2005). With each successive slip event, continued fracturing and reworking of fault material along the rupture planes contributes to the weakening of the plane and surrounding damage zone (Shipton et al., 2006; McKay et al., 2021). Processes such as flash heating (Rice, 2006) and melt lubrication (Di Toro et al., 2006) contribute to weakening during slip. The active weakening mechanisms along the rupture plane influence the rheological response of the affected wall rock and propagation through the fault zone (Kirkpatrick & Shipton, 2009).

The presence of fluids in a system can facilitate additional weakening mechanisms, such as thermal pressurization (Sibson, 1973). In this process, differences in thermal expansion between pore fluids and pore space during frictional heating increases pore fluid pressure, leading to a rapid drop in normal stress (Barras & Brantut, 2025). Other fluid-assisted processes, including reaction

softening or silica gel formation (Onasch et al., 2010), can further reduce fault strength by promoting mineral breakdown and the formation of mechanically weaker phases (White et al., 1980). Alternatively, fluids can contribute to fault healing through pressure solution or precipitation reaction processes, which restore cohesion and strength to the fault (Bos & Spiers, 2002; Yehya & Rice, 2020). The weakening and healing processes at work along a rupture plane produce diagnostic fault rock (micro)structures and geochemical signatures that reflect the conditions of seismic slip.

Such structures include pseudotachylytes, quenched melts from frictional heating, and ultracataclasites, comminution of host rock, that develop along slip planes during rupture (Sibson, 1975). These fault rocks are widely recognized as direct indicators of coseismic slip (Rowe & Griffith, 2015). Intact ultracataclastic veins and pseudotachylytes are rarely preserved within fault zones, due to overprinting from progressive plastic or cataclastic deformation along the fault zone, hydration alteration from the introduction of fluids, or recrystallization (Kirkpatrick & Rowe, 2013; Bestmann et al., 2016; Mancktelow et al., 2022). As such, the structures that are preserved and exposed through exhumation provide key insights into the rupture processes and temporal evolution of seismogenic fault zones (Swanson, 1992). Moreover, studying seismic structures in hydrated fault systems can elucidate the influence of fluids on deformation processes by facilitating element mobility (White et al., 1980; Blacic & Christie, 1984), altering the conditions of earthquake rupture.

Ultracataclastic veins and pseudotachylytes hosted in a deformed granodiorite on the island of Naxos, Greece, provide a natural laboratory to examine these earthquake-induced structures in a hydrated system. Naxos, a classical Miocene extensional metamorphic core complex, has a well-documented tectonic history (e.g., Lister et al., 1984; Vanderhaeghe, 2004; Bessiere et al., 2018),

offering a robust foundation for characterizing fault rock deformation. The structures formed in the upper 200 m of the footwall of the Naxos-Paros Detachment system (NPDS) and record footwall unroofing through the brittle-ductile transition zone into the brittle regime (John & Howard, 1995; Lamont et al., 2019). John and Howard (1995) identified several instances of a mylonitic overprint of the pseudotachylytes, concluding that the Naxos granodiorite experienced alternating periods of ductile deformation and coseismic slip. Bessiere et al. (2018) further reported that the pseudotachylytic veins occur dominantly parallel to ultramylonitic bands, with stretching-perpendicular injection veins. These observations are indicative of a dynamic emplacement history, where the processes controlling the formation, geometry, and growth of the veins remain unresolved.

Although these outcrops are renowned for their pseudotachylyte exposures (John & Howard, 1995; Cao et al., 2013; Lamont et al., 2019), our structural observations reveal that many of these veins are instead ultracataclasites, which did not experience frictional melting, marking a significant reinterpretation of these fault rocks. The first section of this study presents new, detailed field observations of ultracataclastic and pseudotachylytic veins on Naxos and their spatial relationship to the NPDS. The structural data provide the framework for the second portion of this work, in which the mechanisms of nucleation and propagation of these veins are investigated using 2D microstructural and geochemical analyses. Electron backscatter diffraction (EBSD) mapping demonstrates that cataclasis is the primary deformation mechanism linked to vein genesis and injection. Complementary electron microprobe element mapping of the vein material and surrounding host rock porphyroclasts suggests that fluid-induced chemical reactions contribute to localized weakening along the rupture paths. Together, these observations highlight a coupled

mechanical and chemical feedback process operating within the seismic cycle, with implications for understanding the propagation of earthquake rupture in fluid-rich fault zones.

2. Geological setting

2.1 Geology of the Cyclades

The Cycladic archipelago of the central Aegean region (**figure 1**) forms part of the back-arc domain of the Hellenic subduction zone where Alpine convergence between the Eurasian and African plates drove the late Mesozoic-Cenozoic closure of the Neotethyan ocean (Pichon & Angelier, 1979; Jolivet & Brun, 2010). During the Miocene, slab rollback of the African plate triggered extension in the overriding plate, leading to the exhumation of a series of Cordilleran-type metamorphic core complexes via low-angle extensional fault systems (Lister et al., 1984; Brun & Faccenna, 2008; Jolivet & Brun, 2010), including the North Cycladic Detachment System (NCDS; Jolivet et al., 2010), the West Cycladic Detachment System (WCDS; Grasemann et al., 2012) and the NPDS (Gautier et al., 1993; Brichau et al., 2006; Cao et al., 2013). These metamorphic core complexes constitute the Attic-Cycladic Crystalline Massif and expose the three primary tectonostratigraphic units of the massif's nappe stack (Durr et al., 1978). The Cycladic Blueschist Unit (CBU), the dominant unit of this package, is primarily comprised of high-pressure, low-temperature (HP-LT) metasediments and metaigneous rocks, with metavolcanic blocks (metabasalt to metaperidotite) and ophiolitic olistostromes (Blake et al., 1981). The CBU is structurally above the Cycladic Basement, a Paleozoic package of orthogneisses, paragneisses and granitoids (Andriessen et al., 1987; Huet et al., 2009). Both units record two distinct Alpine metamorphic events: M1) Late Cretaceous to Eocene HP-LT metamorphism at eclogite and blueschist facies conditions (Jansen & Schuiling, 1976), and M2) an overprint characterized by

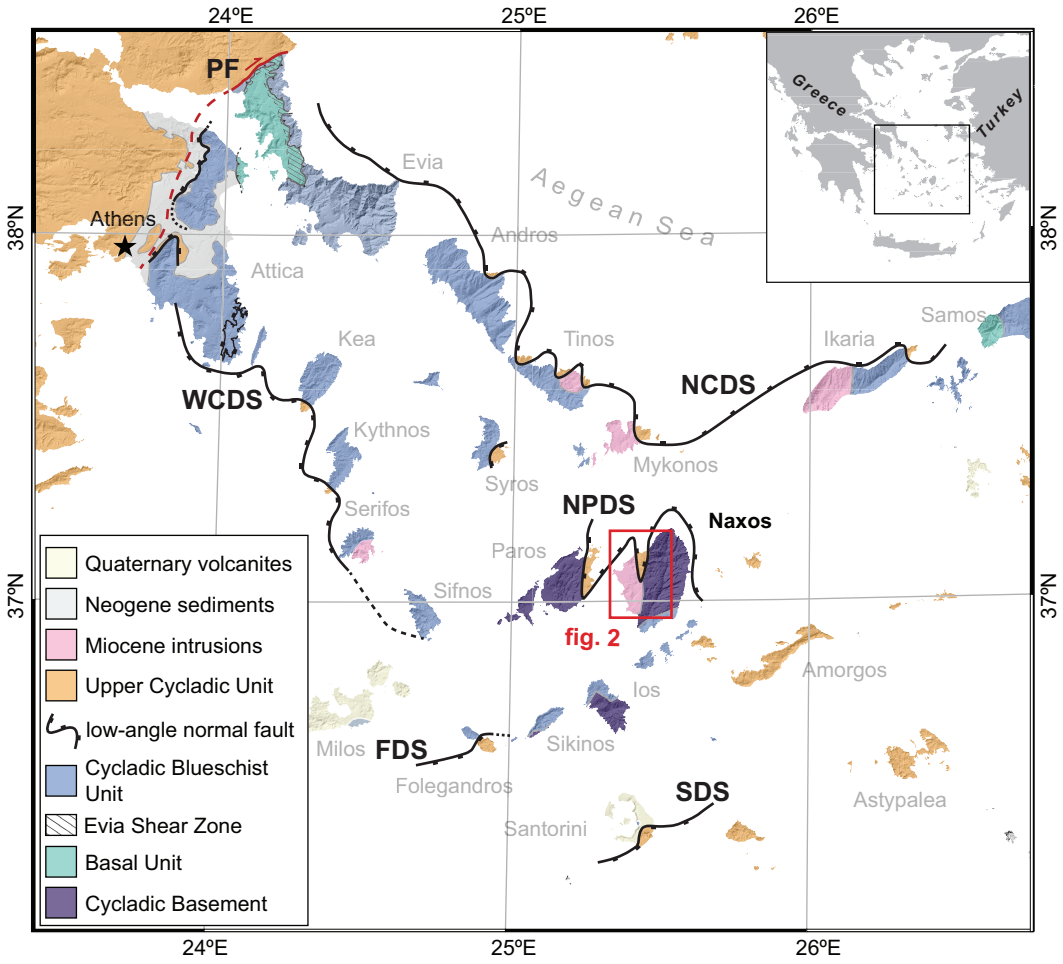

Figure 1. Simplified tectonic map of the Greek Cyclades with the major tectonic units and the regional extensional systems. The map area in figure 2 is outlined by the red box. Inset displays the map of the Aegean Sea with the map area outlined in black. The Pelagonian Fault (PF) is a strike-slip system outlined in red. FDS: Folegandros Detachment System; NCDS: North Cycladic Detachment System; NPDS: Naxos-Paros Detachment System; SDS: Santorini Detachment System; WCDS: West Cycladic Detachment System. Modified from Ducharme et al. (2022) and Bakowsky et al. (2025).

Barrovian-type medium-pressure, medium- to high-temperature metamorphism in the Oligo-Miocene (Andriessen et al., 1979; Altherr et al., 1982). The third tectonostratigraphic unit consists of the Upper Cycladic Unit, a thin sequence of Late Cretaceous low-pressure metamorphic rock, including mafic phyllites, layered amphibolites, and remnants of ophiolitic material, which overlies the CBU and Basement. The upper unit was not subjected to either of the two main metamorphic events recorded within the Cyclades and has been linked to the Pelagonian domain exposed on mainland Greece (Durr et al., 1978; Avigad & Garfunkel, 1989; Katzir et al., 2007).

2.2 Geology of Naxos

Located in the center of the archipelago, Naxos is the largest island of the Greek Cyclades and is dominated by a north-south elongated dome of gneiss and intercalated marble, with a migmatitic core (**figure 1, 2**; Lister et al., 1984; Vanderhaeghe, 2004). The dome is considered part of the CBU, although the migmatite core may be attributed to the Cycladic Basement (e.g., Jolivet et al., 2004; Peillod et al., 2017; Bessiere et al., 2018). Within the dome, concentric metamorphic isograds that show an increase in temperature towards the central core, were mapped by Jansen and Schuiling (1976). Feenstra (1985) corroborated this metamorphic progression by mapping the diaspor corundum reaction in metabauxite deposits within the marble units of the dome, demonstrating an increase in corundite towards the core (Feenstra & Wunder, 2002). Conditions of M1 at 380°C-475°C and >9 kbar are preserved in blueschist facies mineral assemblages (e.g., glaucophane-epidote-chlorite-albite; Jansen & Schuiling, 1976; Buick & Holland, 1989; Keay et al., 2001; Duchêne et al., 2006, Lamont et al., 2019). Peak M2 conditions generated partial melting and migmatization at ~700°C and 8.5 kbar (Jansen & Schuiling, 1976; Buick & Holland, 1989; Duchêne et al., 2006). Lamont et al. (2019) delineated a third sillimanite facies metamorphic event

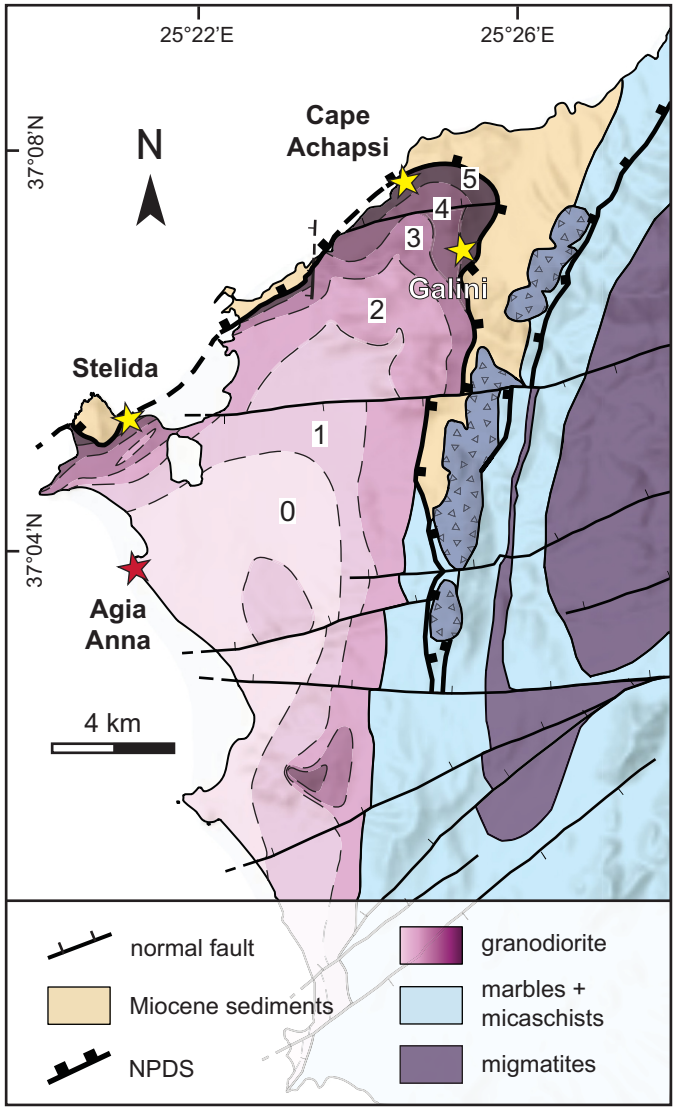

Figure 2. Simplified geological map of western Naxos, showing zones 0-5 of the granodiorite strain gradient (pink), modified after Bessiere et al. (2018). Darker pink indicates higher strain. Talus: blue triangular pattern. Ultracataclasite sample locations noted by yellow stars: Stelida Peninsula, Cape Achapsi, Galini. Undeformed granite sample collected at Agia Anna noted by red star. NPDS: Naxos-Paros Detachment System.

(M3) resulting from near-isothermal decompression in the migmatite core to conditions of ~5-6 kbar and 700-730°C. Zircon U-Pb geochronology by Keay et al. (2001) indicates anatexis occurred between c. 21 Ma and c. 17 Ma, followed by exhumation-related cooling below 500°C between c. 19 Ma and c. 15 Ma determined from K/Ar dating (Andriessen et al., 1979; Wijbrans & McDougall, 1988; Duchêne et al., 2006). This coincides with the results of Vanderhaeghe et al. (2018), who constrained formation of the Naxos dome by diapirism between c. 16-13 Ma, using U-Pb geochronology of granitic dikes hosted in the migmatites. Repeated metamorphism and the latest exhumation of Naxos involved significant fluid flow, which likely promoted deformation-metamorphism feedbacks. Analysis of fluid inclusions from rocks in the core established three distinct generations of fluid sources (Siebenaller et al., 2013): 1) CO_2-rich fluids and high-salinity brines originated from metamorphic reactions and crystallizing magmas during M2 metamorphism, 2) upper crustal low-temperature metamorphic fluids produced during exhumation through the brittle-ductile transition, and 3) meteoric fluids trapped during late brittle deformation between c. 10.5 Ma and c. 9.2 Ma.

On the western side of the island, a Miocene granodioritic intrusion with a hornblende-biotite monzogranite core was syn-tectonically emplaced at crystallization temperatures of 650-680°C between c. 15 and 11 Ma (**figure 2**; Jansen & Schuiling, 1976; Altherr et al., 1982; Henjes-Kunst et al., 1988; Pe-Piper et al., 1997; Pe-Piper, 2000; Keay et al., 2001; Bolhar et al., 2010; Bessiere et al., 2018). The I-type granitoid subsequently cooled rapidly to <60°C by c. 9 Ma, as determined from fission track dating of apatite and zircon (Andriessen et al., 1979; Altherr et al., 1982; Hejl et al., 2002; Brichau et al., 2006; Seward et al., 2009).

The metamorphic dome and granitoid are separated from overlying Miocene marine deposits and turbidites by the crustal-scale NPDS (Jansen, 1973). On Naxos, the detachment is a

shallowly NE-dipping extensional shear zone, folded along a NNE-SSW axis, which facilitated the tectonic exhumation of the core complex between c. 13-9 Ma (Buick, 1991; Gautier et al., 1993; Mancktelow et al., 2016). Despite being well-defined, there are only remnant exposures of the detachment plane along the northeastern and western edges of the island. Intensity of the deformation in the granodiorite increases towards the detachment surface (Gautier et al., 1993), and the strain gradient was further refined into six zones by Bessiere et al. (2018; **figure 2**). The lowest strain zone (zone 0) on the southwestern coast has an isotropic magmatic fabric and undeformed matrix (**figure S1a)**. In zone 1, an anisotropic fabric is developed, with a weak N-S stretching lineation. The first instances of tectonic structures in the granodiorite matrix, including sheared and boudinaged feldspars are indicative of zone 2, which occurs ~1000 m below the detachment contact. Zone 3 is defined by the appearance of shear bands and a strong stretching lineation; the structure is considered protomylonitic. Foliation intensifies towards the detachment plane in zones 4 and 5, producing an SCC' fabric with top-to-N kinematics (Urai et al., 1990; Gautier et al., 1993). In the immediate footwall of the detachment, the structure locally progresses from mylonitic to ultramylonitic, coupled with an increase in the thickness and frequency of shear banding. In the highest strain zone (5), 'pseudotachylytic' veins overprint the ductile fabric and mylonite shear bands (Jansen, 1977; John & Howard, 1995; Bessiere et al., 2018). Formation of the pseudotachylytes likely correlates to the transition from the ductile to brittle-ductile behavior of the crust. These veins have been dated at c. 9.9 Ma by Andriessen et al. (1979) via whole rock K-Ar analysis, confirming their late-stage genesis linked to extensional deformation. Brittle deformation is marked by ultracataclasis and high-angle normal faulting, which segments the intrusion particularly in the north. At the base of the detachment plane, a ~50 m-wide extensively chloritized cataclastic zone (**figure S1b**) completely overprints any ductile fabric (Buick, 1991).

The intense chloritization at the NPDS plane reflects late-stage low temperature hydrothermal alteration associated with infiltration of meteoric fluids (Cao et al., 2017). This is supported by δD values of the NPDS fault gouge (-89‰ to -95‰; Mancktelow et al., 2016), which confirm a meteoric fluid source during clay gouge formation. Collectively, these structures record the transition from solid-state ductile to brittle conditions during displacement along the detachment.

3. Field and petrographic observations

3.1 Vein set classification

The Naxos granodiorite has a primary assemblage of medium-grained (0.5-3 mm diameter) albite (25-35%), quartz (25%), potassium feldspar (15%) and biotite (12%) phenocrysts with accessory chlorite (6%), hornblende (4%) and titanite (<1%) (**figure S1a, S2**). Proximal to the fault plane of the detachment, foliation is developed, (sub)parallel to the detachment (~240°/36° NW) in the high strain (5) zone (**figure 3**). The foliation is defined by elongated potassium feldspar crystals (up to 11 cm in length), stretched biotite, and sigmoidal shaped quartz crystals (0.5-2 mm; **figure 4a**). A stretching lineation that trends ~351° is present in the north and is most apparent as aligned 1 mm-long biotite laths.

The deformed granodiorite hosts ultracataclastic and pseudotachylytic veins at three exposures within the highest strain zone (Bessiere et al., 2018): 1) at Cape Achapsi, 2) near the village of Galini, and 3) along the eastern Stelida Peninsula (**figure 2**). At Cape Achapsi the detachment plane is clearly exposed and dips ~20° to the north. Here, the granodiorite is finer grained (<1 mm diameter matrix) and pale green from intense chloritization, with multiple generations of extensive cataclasis marked by lenses of reworked cataclastic material and discolored light grey ultracataclastic veinlets within larger dark grey to black veins (**figure S1b**). The granodiorite at the Galini exposure is also significantly chloritized, however, there is less

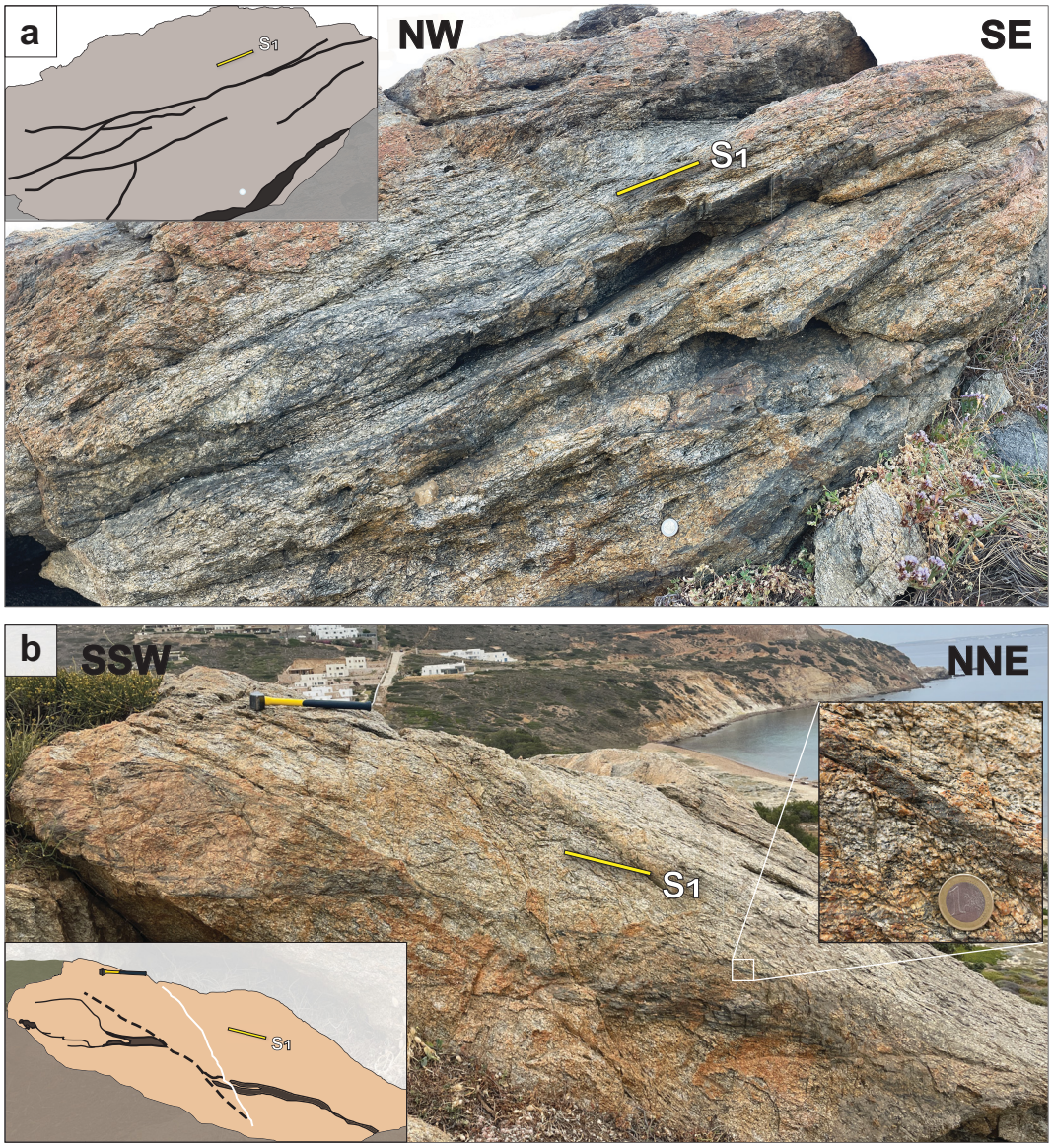

Figure 3. Representative field photos of deformed granodiorite outcrops on the Stelida Peninsula with ultracataclastic vein networks. The tectonic foliation (S1) of the host rock is shown in yellow. (**a**) An outcrop showing sinuous ultracataclastic veins (black lines in top left sketch) mainly sub-parallel to the foliation (S1; 240°/36°) of the host rock. Abundant anastomosing veinlets (0.5-1.2 cm) relay between larger veins (3-6 cm thick) (UTM: 353657 E, 4105928 N). (**b**) In the center of an outcrop, a series of thick foliation-(sub)parallel veins (black lines in bottom left sketch) are offset by a vein steeper than foliation (dashed black line in sketch). A late fracture (white line in sketch) also offsets the foliation parallel veins. The right inset photo displays the ultracataclastic material within the veins (UTM: 353683 E, 4105854 N). 2€ coin for scale in (a): 26 mm diameter. Hammer for scale in (b): 36 cm length. 1€ coin for scale in inset of (b): 23 mm diameter.

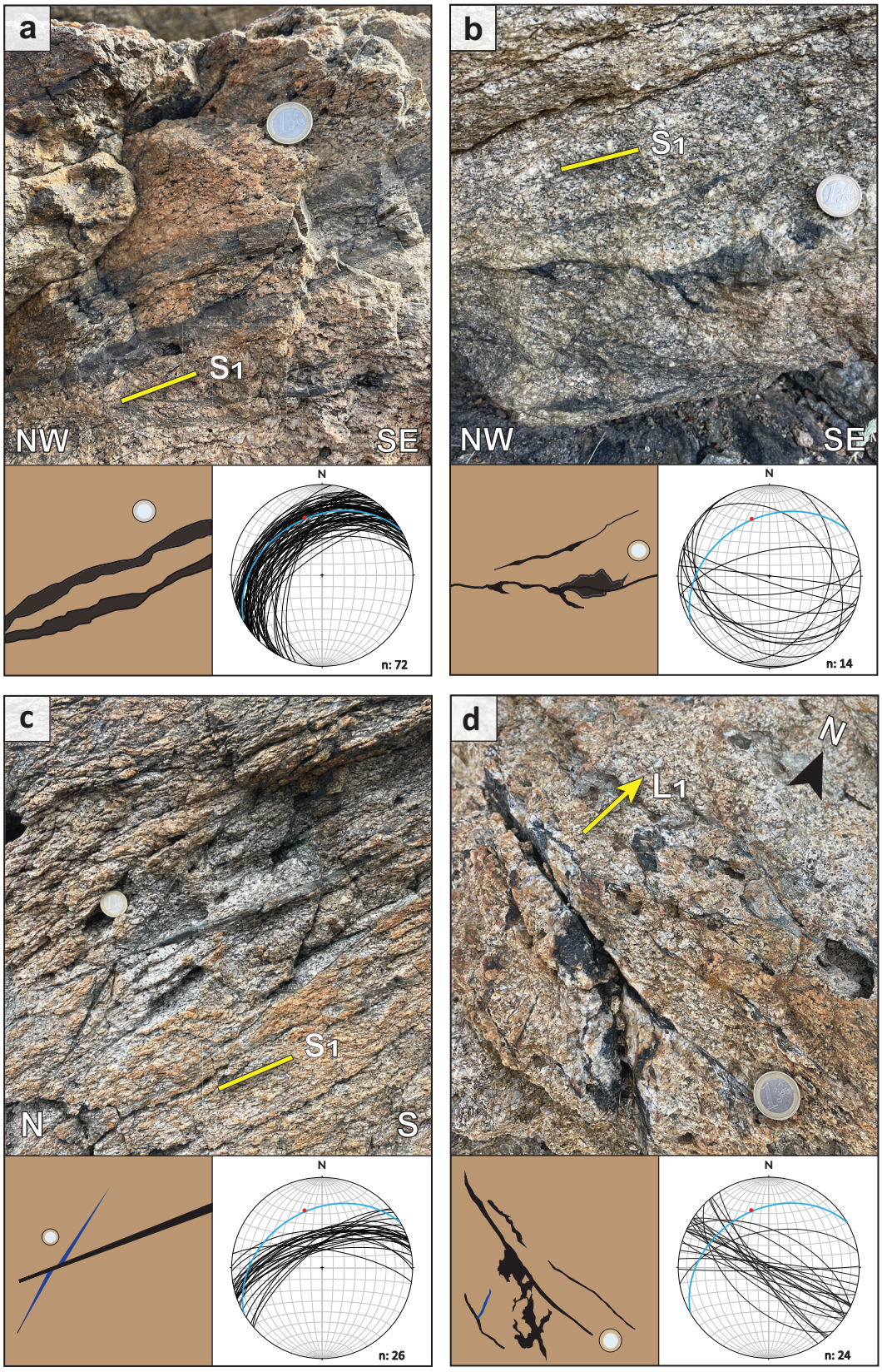
a
S1
NW
SE
N
n: 72
b
S1
NW
SE
N
n: 14
c
S1
N
S
N
n: 26
d
N
L1
N
n: 24

Figure 4. Representative field photos and associated lower hemisphere equal area stereonets for each ultracataclastic vein set types. On stereonets, a representative host rock foliation is in blue and a stretching lineation is in red. (**a**) Foliation (S1) (sub)parallel veins (353665 E, 4105954 N). (**b**) Injection veins protruding from the slip surface plane (353668 E, 4105940 N). (**c**) Vein steeper than foliation, offset by a foliation-parallel vein; shown as dark blue and black veins in inset, respectively (353745 E, 4105935 N). (**d**) Note photo is in plan view. Veins and fractures crosscutting the host rock lineation (L1) at 120°. These oblique veins are highlighted in the inset sketch in black. Also shown is an oblique vein cross-cutting a foliation-parallel vein (blue in subset) at the bottom right (353638 E, 4105938 N). 1€ coin for scale (a-d): 23 mm diameter.

overall cataclasis, and more discrete slip surfaces are preserved that account for ~3-5% of the exposure (**figure S1c**). At the surface, the granodiorite exposure at Stelida is ~100 m from the mapped trace of the detachment. The granodiorite is light grey with larger porphyroclasts (up to 2.5 mm), a pervasive stretching lineation (17°-345°), and cataclasis limited to localized rupture paths. At all three locations, the ultracataclastic material is fine-grained (<2 mm), light to dark grey, and of the same composition as the host rock, with occasional 2 mm-diameter fractured and rotated clasts embedded in the fine-grained matrix. In contrast, the pseudotachylytic material is darker with branching offshoots, and often vitreous with conchoidal fracturing (**figure S3a**). Often the ultracataclastic veins will display local zones of darker, glassy pseudotachylytic material. Due to the fine-grained and homogeneous nature of the ultracataclastic veins, it can be difficult to distinguish between the two types of fault rocks in the field. Based on vein set characteristics such as orientation, length, and cross-cutting relationships with other veins or the host rock at these locations, three vein types were documented: i) foliation-(sub)parallel veins, ii) veins steeper than foliation, and iii) veins striking oblique to, and crosscutting, foliation (**figure 4**). In the following, we describe the macro-scale observations and examine the associated deformation structures of each type.

i) Foliation-(sub)parallel veins (**figure 4a**), oriented ~235°/35° NW, occur directly along primary slip surfaces and are consistently thicker (2-7 cm) than the other vein set types. At Stelida, these veins are irregularly spaced, from 3 cm and up to 0.5 m apart, and vary significantly in length, with many spanning the length (>10 m) of an exposed granodiorite outcrop. They anastomose, often with thin (1 cm) relay veins between thick branches (**figure 3a**). The vein margins form a discrete boundary with the host rock, however minor bleaching of the host rock was observed up to 1.5 cm away from the vein margins. Material within the vein is fine-grained (<0.1-1.5 mm); the

majority of individual grains are too small to be distinguished in the field. The veins range in color from dark grey to black. Some of the darker vein material appears vitreous with conchoidal fracturing, indicative of frictional melt material. Commonly accompanying the foliation-parallel veins are thin (up to 2.5 cm) offshoots of ultracataclastic material at a high angle to the main slip surfaces. These injection veins (**figure 4b**) appear homogenous, glassy, and rarely contain inclusions of larger (1-2 mm) clasts. The vein geometry is typically triangular shaped in two dimensions, tapering to a point, and 0.5-3.5 cm in length. Many of the mapped injection veins curve into the host rock foliation plane (**figure 4b**).

ii) Veins oriented steeper than foliation strike ~255°, at a similar orientation to foliation-parallel veins (see stereonets of **figure 4a, b**), and consistently dip between 60-73° NNW. These veins occur along straight and discrete rupture surfaces. Veins that anastomose and smaller veinlets were not considered part of this subset. The steeper veins are thinner (1-3.5 cm) and crosscut the foliation-parallel veins (**figure 3b; 4c**), possibly suggesting multiple pulses of slip and pulverization.

iii) A series of thin (2 cm) ultracataclastic veins and fractures striking ~127° and dipping between 65-78° NE crosscut the tectonic foliation and the other vein types at the Stelida and Galini outcrops (**figure 4d**). These vein and fracture sets are spaced 3-5 cm apart and are randomly distributed along the outcrops at both locations. The material is vitreous and black, with a 0.5-1 cm bleached margin in the host rock.

The brittle structures preserved within the highest strain zone of the pluton provide a record of progressive faulting along the detachment. At the detachment plane, the immediate footwall is heavily compromised by fault gouge and cataclastic overprinting, eliminating or reworking the majority of discrete veining, as seen at Cape Achapsi. Farther (50-100 m) from the detachment, at

the Galini and Stelida sites, deformation is localized into distinct slip planes. We observed polished surfaces with striations at both locations, plunging ~29° towards ~330° (**figure S1d**). The three vein set types and their spatial relationship to the detachment and the cataclastic zone are illustrated in **figure 5**.

3.2 Microstructure analyses

Ultracataclastic vein samples from the three exposures in strain zone 5 (Bessiere et al., 2018), and a relatively undeformed granodiorite sample (**figure 2**; UTM: 353637 E, 4103387 N) from Agia Anna in strain zone 0 were collected for detailed microstructural analysis. Thin sections were cut perpendicular to foliation and parallel to the stretching lineation, except for samples Bp4 and Bp6, which were cut perpendicular to lineation.

The primary magmatic assemblage of the granodiorite sampled from zone 0 (**figure 6a**) comprises albite, potassium feldspar, quartz and biotite, with minor hornblende. Despite being sampled from the undeformed zone, petrographic observations of the magmatic assemblage revealed evidence of minor deformation and anisotropy. Albite grains (0.1-3 mm) are blocky and euhedral, with some compositional core-to-rim zoning and fluid inclusions near the crystal margins (**figure S3b**). Tectonic structures present in the albite phenocrysts include fracturing and patchy extinction. The potassium feldspar is dominantly orthoclase (90%) with lesser amounts of microcline (10%). The orthoclase phenocrysts are subhedral, elongated, and the largest crystals in the matrix (up to 4 mm) with curved to serrated grain boundaries. The potassium feldspar also exhibits deformation in the form of patchy extinction, fracturing, and subgrain development towards grain margins. Quartz phenocrysts (0.1-2 mm) range from polygonal grains with straight grain boundaries to anhedral grains with curved and irregular boundaries. The grains show undulose extinction and fracturing, where the fractures and grain boundaries are often lined with

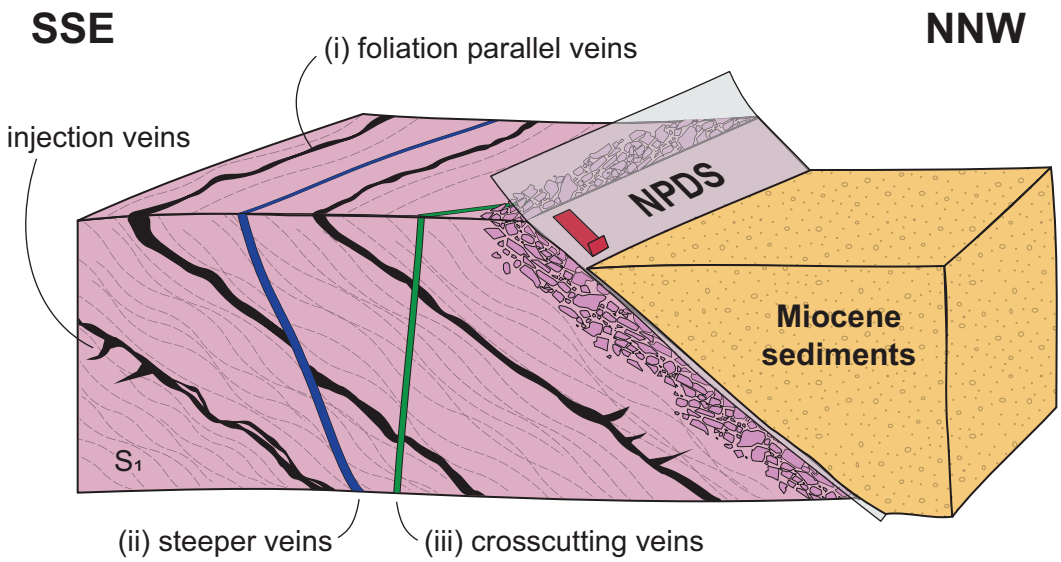

Figure 5. Schematic block model of the three ultracataclastic vein set types (i-iii) hosted in the granodiorite (pink) of the immediate footwall of the Naxos-Paros Detachment. Note the cataclastic zone of host rock fragments below the detachment plane. The injection veins occur along the foliation parallel veins and are included in set (i). Foliation (S_1) illustrated by undulating dashed lines.

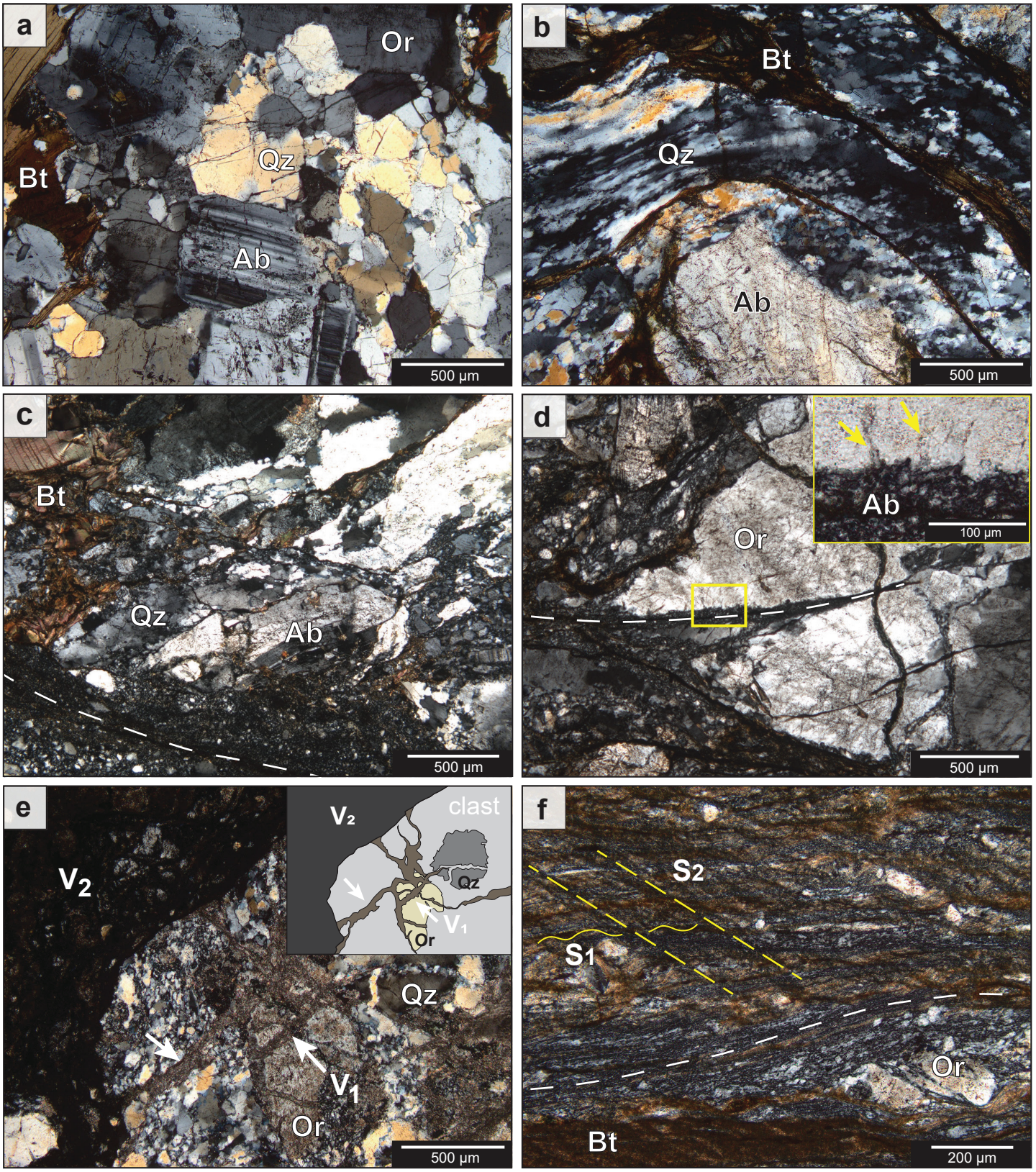
a
Or
Bt
Qz
Ab
500 µm
b
Bt
Qz
Ab
500 µm
c
Bt
Qz
Ab
500 µm
d
Ab
100 µm
Or
500 µm
e
V2
clast
V2
Qz
V1
Or
Qz
V1
Or
500 µm
f
S2
S1
Or
Bt
200 µm

Figure 6. Photomicrographs (XPL) of Naxos ultracataclasite microstructures. Quartz: Qz, albite: Ab, orthoclase: Or, biotite: Bt. (**a**) Low-strain granodiorite (zone 0), with minor fracturing, fluid inclusions and indistinct grain boundaries unrelated to cataclasis (353637 E, 4103387 N). (b-f) Images are proximal to vein margins and were taken from samples in deformation zone 5. (**b**) Dynamically recrystallized grains of quartz porphyroclasts define foliation and flow around feldspar clasts in the host rock (353649 E, 4105948 N). (**c**) Quartz-rich ultracataclastic vein (white dashed line) cutting through strongly fractured quartz and albite clasts. The albite clast displays bent and tapered twins towards the vein margin. Area of EBSD map Bp4 (353649 E, 4105948 N). (**d**) Albite-rich ultracataclastic vein (white dashed line) propagated and terminated into host orthoclase clast. Inset (yellow box): cuspate phase boundary between orthoclase clast and albite aggregates. Yellow arrows point to fluid inclusions in the orthoclase. Area of EBSD map Cll2 (353649 E, 4105948 N). (**e**) Evidence of multiple genera-tions of cataclasis, sericitization, and fracturing of host grains within a clast at the periphery of an ultracataclastic vein (358684 E, 4110375 N). White arrows point to older ultracataclastic veinlets preserved in the clast. Inset: schematic of photomicrograph, highlighting the clast (light grey) within the latest generation of veining (V2). Older veinlet material is outlined in dark grey (V1). The fractured orthoclase porphyroclast is in beige. (**f**) Biotite-rich ultracataclastic veins parallel to foliation (S1), with a crenulation cleavage (S2) (353651 E, 4105925 N).

tabular biotite crystals. The granodiorite also displays a slight alignment of blocky biotite laths (0.25-1.75 mm), recording the onset of the anisotropic fabric characteristic of the zone 1 granodiorite. Minor dark green subhedral hornblende is adjacent to, or intergrown with, larger biotite crystals.

In the highest strain zone, the granodiorite matrix has a transitional microstructure, where the magmatic fabric is recognizable but extensively overprinted by local brittle and ductile structures. The rock has an overall finer grained matrix compared to the low-strain granodiorite, and is mostly comprised of albite, quartz and orthoclase aggregates. Relict porphyroclasts of these phases preserve structures indicative of both crystal-plastic and brittle processes. Albite porphyroclasts are subhedral (50 μm-2 mm), with pervasive micrometer-scale fracturing including bookshelf micro-fracturing, along with irregular grain boundaries and patchy extinction (**figure 6b**). The porphyroclasts also exhibit pericline and albite twinning that are both tapered and bent (**figure 6c**). Orthoclase clasts (0.5-3 mm) are mostly elongated subhedral to anhedral, with some sigmoidal shaped grains (**figure S3c**). The clast grain boundaries are commonly curved but can be irregular and diffuse. Orthoclase clasts crosscut by the veins show an irregular to cuspate phase boundary with fine-grained albite aggregates (2-45 μm; **figure 6d**). The orthoclase clasts are porous (**figure 6d**) and significantly fractured, also displaying bookshelf micro-fracturing (**figure S3d**). Fluid inclusions in the orthoclase clasts concentrate near regions of extensive fracturing and towards clast rims (white arrows in **figure 6d**). Quartz grains are inequigranular, with a range of grain size from 40 μm-1 mm. Interlobate to amoeboid quartz grain shapes (**figures 6b, c**) are a result of subgrain rotation and grain boundary migration recrystallization. The dynamically recrystallized quartz grains display a shape preferred orientation defining the foliation around the larger feldspar porphyroclasts (50 μm-2 mm; **figure 6b**). Irregular grains of biotite reside between

the main phases and form stretched ribbons that are boudinaged (**figure 6b**). Relict biotite clasts vary from blocky to lenticular or sigmoidal shaped, occasionally showing kink banding in the clasts (**figure 6c**).

Near the ultracataclastic vein margins, host rock porphyroclasts of albite, orthoclase and quartz are highly fractured with increasing apparent subgrain density towards the veins (**figure 6c, d**). The vein material itself is homogeneous and comprised of rounded to subrounded, equant clasts (5-70 μm), with occasional angular fragments particularly towards vein margins (**figure 6c**). The ultracataclastic grains have slightly curved to irregular grain boundaries and few distinguishable subgrains and fractures in isolated larger porphyroclasts. Some of the ultracataclastic veins contain rounded clusters of host matrix and porphyroclasts, which preserve remnants of older vein networks (**figure 6e**). In the reworked clusters, or clasts, the large porphyroclasts show patchy extinction and irregular grain boundaries. The older generations of ultracataclastic veinlets are thin (5-20 μm), light grey and sericitized, propagating through relict porphyroclasts and matrix, terminating at the clast boundaries (**figure 6e**). The older veinlets are generally oblique to the orientations of the surrounding dark ultracataclasites. Reworked clasts are most prevalent in samples collected from the cataclastic zone at Cape Achapsi, and are typically larger, ranging from 10 μm to 3.7 mm in width. Vein samples collected further from the detachment at Stelida contain limited, small (55 μm in length) examples of multi-generational clasts.

Ultracataclastic vein boundaries vary from sharp, which are characteristic of ultrafine-grained (>30 μm) dendritic, biotite-rich veins (**figure S3a, e**), to gradational with a damage zone (~150 μm wide) of subrounded to subangular fine-grained fragments (**figure 6c**). Thin (40-65 μm) chlorite veins are often present proximal to the ultracataclastic veins, particularly as a rim along the outer edges of the veins (**figure S3a**). In several samples coarse-grained (40-450 μm),

subhedral biotite and hornblende concentrate on the perimeter of the veins. A sequence of foliation-parallel, biotite-rich veins exhibit repeated, equally-spaced, apparent dark planes, oriented obliquely to the foliation (28°-33°), suggesting a crenulation cleavage within the veins (**figure 6f**). Offshoot veinlets from the foliation-parallel veins are consistently thin (35-180 μm), dark and crenulated (**figure S3e**). In thin section, the steeper-than-host rock foliation veins that belong to the second vein subset are more biotite-rich (85%), with very fine (~20 μm) feldspar and quartz clasts, and between 120-550 μm thick. They display diffuse vein boundaries, with a rim of small feldspar and quartz grains (<50 μm) lining the vein. Bands of darker material within the veins are visible and intensifies towards the vein margin. Some smaller (20-60 μm) foliation-(sub)parallel veins overprint the steeper veins (**figure S3f**). The third vein subset was not observed in our samples.

4. Analytical methods

High-contrast backscattered electron (BSE) imaging and EBSD mapping were employed to qualitatively and quantitatively characterize the structural and compositional features of the ultracataclastic veins and their surrounding host rock. Four polished thin sections were prepared from one hand sample for microstructural analysis. The investigated hand sample was selected as it contained multiple vein tips terminating in the host granodiorite. Samples All and Cll were cut along the XZ plane (normal to foliation and parallel to the stretching lineation; notation: ll), and samples Bp and Dp were cut along the XY plane (normal to foliation and perpendicular to stretching lineation; notation: p). Thin sections were chemo-mechanically polished with a colloidal silica suspension and carbon-coated (~10 nm thickness) to prevent charging. Scanning electron microscopy (SEM) BSE imaging and EBSD mapping were conducted using a high-resolution

field-emission Zeiss SEM Merlin (Carl Zeiss Microscopy, Germany) equipped with a Hikari (EDAX, USA) EBSD detector at the Max-Planck-Institut für Nachhaltige Materialien (MPI SusMat, Düsseldorf, Germany). For BSE imaging, analytical conditions were set to a 15 kV accelerating voltage, a 5.0-7.0 nA beam current and a working distance between 9.0-10.0 mm. EBSD analyses were performed at an accelerating voltage of 20-30 kV and a 7.0 nA beam current. Thin sections were tilted at a 70° angle and mapped at a working distance of 15.0-16.7 mm using a step size of 1.25-2.5 μm, and 8×8 camera binning. Individual sample EBSD parameters are listed in **Table S1**. Acquired maps were subsequently re-indexed with spherical indexing using the EDAX OIM Analysis software (Hielscher et al., 2019; Lenthe et al., 2019). Spherical indexing was performed using a bandwidth of 127, applying the dynamic background and auto-brightness contrast functions, as well as the non-local pattern averaging reindexing (NLPAR) function with a decay of 1.50 to improve pattern quality. A chemical indexing scan (ChI Scan) was also simultaneously applied, which combines the EBSD data with elemental information acquired from energy dispersive (EDS) X-ray spectroscopy to facilitate phase identification and enable accurate microstructural analysis of all phases. The re-indexed EBSD data was cleaned using the OIM Analysis software, combining the neighbor orientation correlation (clean-up level: 3) and confidence index standardization (CI: 0.1) functions. Further EBSD data processing was completed using the open source MTEX v5.10.2 toolbox (Bachman et al., 2010; https://mtex-toolbox.github.io/index) for MATLAB. Grains were reconstructed with a minimum misorientation threshold value of 15° for grain boundaries and 2° for subgrain boundaries. Crystallographic orientation maps are color coded according to the inverse pole figure legend, using the ipfHSVKey colormap in MTEX for each phase. All pole figures are lower hemisphere, equal area projections, oriented with the horizontal axis subparallel to the trace of the tectonic foliation.

Following EBSD mapping, complementary geochemical analyses were conducted on the same thin sections (All, Bp, Cll, Dp) to determine the major element distribution and mineral compositions proximal to, and within, the ultracataclastic veins. Preliminary elemental maps were produced using an IXRF Atlas micro-XRF (X-ray fluorescence) spectrometer housed at the Fipke Laboratory for Trace Element Research (FiLTER) at the University of British Columbia-Okanagan. The maps were acquired using an accelerating voltage of 50 kV, beam current of 800 μA, a dwell time of 8 ms, and a spot size of 25 μm. The micro-XRF compositional maps were processed and calibrated using XMapTools v4.3 (Lanari et al., 2014), where spot analyses were used as internal standards. X-ray chemical maps from electron microprobe analysis (EMPA) were produced to assess spatial chemical variations within individual grains. Maps of ten elements (Si, Al, Fe, Mg, Ti, Sr, Na, Ca, K, Ba) were obtained using the JEOL JXA-8230 Superprobe at the University of Ottawa MicroAnalysis Laboratory. The microprobe was operated with a voltage of 20 kV, and a beam current of 200 nA. Pixel size was set to 0.5×0.5 μm, with an acquisition time of 150 ms per pixel. XMapTools was used to visualize EMPA maps with an inverted version of the scientific color map 'nuuk' (Crameri, 2018) and to extract sample spot and transect values. Representative feldspar spot analyses are presented on a compositional ternary diagram, plotted using the MinPlot program for MATLAB (Walters, 2022).

5. Results

5.1 Microstructural results

To determine the deformation mechanisms related to vein nucleation and injection in the Naxos granodiorite, EBSD mapping targeted host rock porphyroclasts that are crosscut by foliation-parallel ultracataclastic veins. Grain and phase boundary maps of albite, orthoclase, and

quartz in each map region are presented in **figure 7** (samples Bp4 and Cll2) and supplementary **figure S4** (samples Bp6 and Dp3). Maps Bp4 and Bp6 are two separate target areas on the same thin section. The thin section utilized for EBSD mapping was produced from a hand sample collected from the Stelida exposure (353649 E, 4105948 N). The four EBSD map areas capture the most intact examples of ultracataclastic vein material, showing minimal evidence of subsequent overprinting. The selected map areas retain microstructures related to vein propagation, allowing for a detailed investigation of the deformation processes operating along the veins and in the surrounding host rock damage zone.

The grain boundary maps display a heterogeneous grain size distribution in both the host rock porphyroclasts and the vein material. The host rock consists of large (up to 1.4 mm in diameter) sub-angular to sub-rounded feldspar and quartz porphyroclasts, which are strongly fractured, producing fragments ranging from 1 μm to 75 μm. The average fragment size decreases progressively towards the vein margins. Grains within the ultracataclastic veins have a mean diameter of 4.5 μm, with occasional larger grains reaching up to 97 μm in width.

5.1.1 Host rock porphyroclasts

Microstructures occurring in the host rock porphyroclasts are indicative of both crystal-plastic and brittle deformation. The orthoclase and albite porphyroclasts exhibit irregular to serrated, high-angle grain boundaries (HAGBs). Feldspar porphyroclasts are heavily fragmented, with fracturing that increases adjacent to vein margins, as displayed by the elongated albite porphyroclast in **figure 7a**, with fine-grained albite material (<60 μm) along the vein margin. The orthoclase grains are typically interlocked, showing a puzzle-like structure with minor dextral

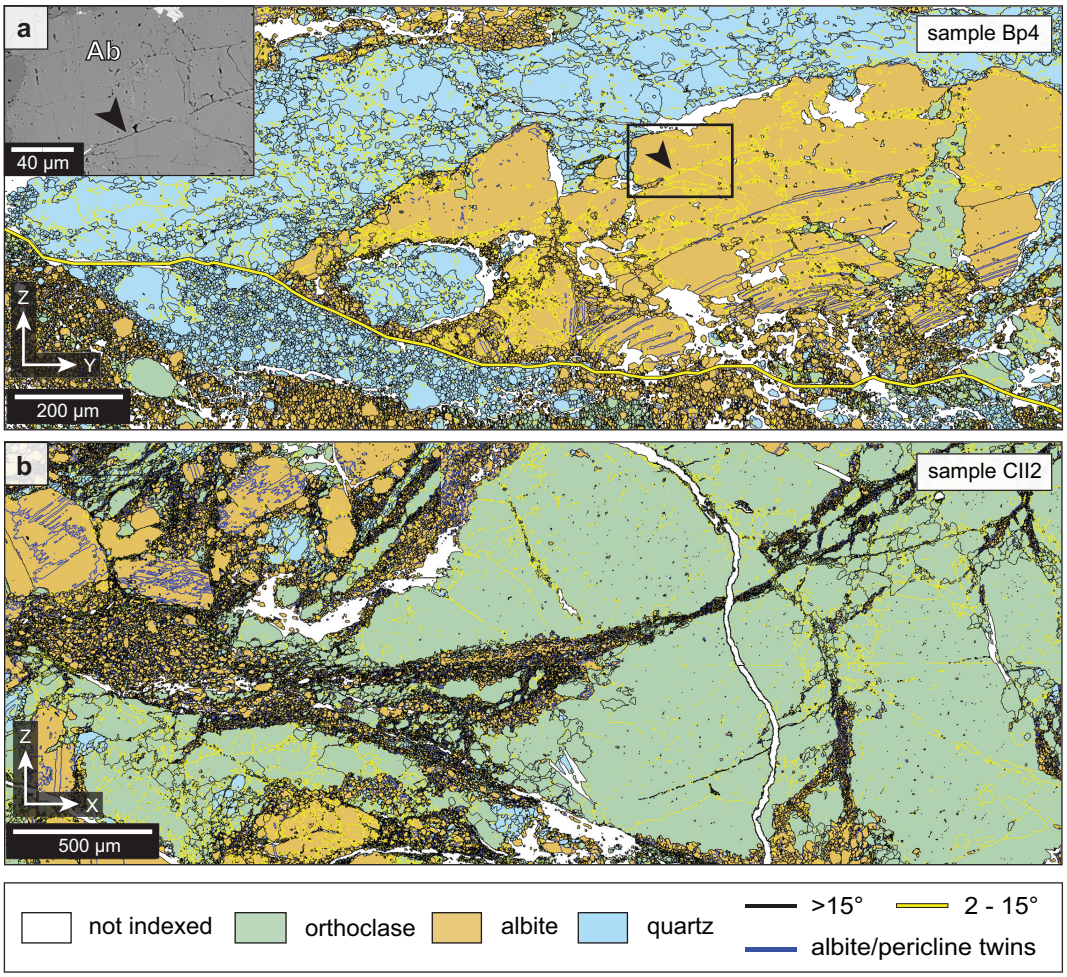

Figure 7. EBSD phase maps of albite, orthoclase and quartz microstructures along ultracataclastic vein margins. Thin section of sample Bp4 (a) is cut perpendicular to lineation, and thin section of sample Cll2 (b) is cut parallel to lineation. The Y- (horizontal) axis is parallel to foliation. Low-angle grain boundaries (LAGBs) are outlined in yellow and twins in albite are outlined in dark blue. (**a**) Albite porphyroclast in sample Bp4 with twins parallel to the c-axis but curved towards the vein rupture path (bottom left). Approximate vein margin is noted by the yellow line. Albite and quartz LAGBS are concentrated proximal to the vein. Fragment fraction increases, and grain size reduces, towards the vein. Inset: BSE image of margin of albite porphyroclast in EBSD map Bp4. Structures in the image suggest boundaries identified as LAGBs in the EBSD map are instead micro-fractures (black arrows). (**b**) Albite rich ultracataclastic material propagating into a fractured orthoclase porphyroclast in sample Cll2. LABGs in albite and orthoclase clasts increase towards outer rims and veins.

displacement between some fragments (**figure 7b**). The ultracataclastic vein tip (**figure 7b**) appears to terminate between the large orthoclase fragments, with fractures originating outward from the tip. Fine-grained albite infills the fractures between the orthoclase clasts at the vein tip (**figure 7b**). Deformation within the feldspar porphyroclasts is further evinced by the presence of mechanical twinning. Straight, polysynthetic and tapered twinning (blue outline in grain maps) in albite is observed parallel to the longest grain axis, with certain twin planes curving and bending towards vein margins (**figure 7a**). Carlsbad twinning in the mapped orthoclase is observed only in a few instances within the host rock and is not highlighted in the grain maps. Quartz porphyroclasts distal from the vein margins are smaller than the feldspar clasts (35-210 μm in width) and have irregular to amoeboid grain shapes. In contrast to the feldspar porphyroclasts, they display a shape preferred orientation, with grains elongated sub-parallel to host rock foliation (**figure 7a; S4a, b**). The quartz porphyroclasts are less fractured than the feldspar clasts. Fractures concentrate towards grain boundaries and become more frequent towards the vein margins. Dauphiné twin boundaries are pervasive in both large porphyroclasts and small fragments towards the vein margins. The twin boundaries are irregular to curved and do not display a systematic arrangement.

Clasts of all three phases exhibit low-angle grain boundaries (LAGB; 2-15°), with density increasing towards clast rims and fractures. The LAGBs also concentrate towards vein margins, most prominently observed in the central albite clasts (575 μm-1.2 mm) of maps Bp4 (**figure 7a**) and Dp3 (**figure S4b**). Longer LAGBs in orthoclase, albite and quartz clasts, with lengths of up to ~240 μm, are preferentially oriented sub-parallel to foliation. Within the elongated albite clast shown in **figure 7a,** a series of stacked, parallel LAGBs align with the orientation of the deformed albite twin boundaries. Shorter LAGBs oriented obliquely to the twin boundaries, connect the stacked LAGBs. Backscattered electron images of these LAGBs (**figure 7a**) suggest that most of

the boundaries identified as LAGBs in the grain maps of the feldspars are instead intracrystalline micro-fractures. The fractures appear as sharp discontinuities terminating at grain boundaries, with minor variations in crystal lattice orientations towards the cracks, shown in both BSE imaging and grain orientation deviation maps (**figure 8a**). LAGBs within the quartz clasts are straight to slightly curved and are also often subparallel to the elongated grain axis. Unlike the LAGBs of the feldspar porphyroclasts, these LAGBs represent subgrain boundaries, showing no sharp fractures in BSE images and exhibiting continuous misorientation patterns within the subgrain areas.

Grain orientation deviation maps highlight lattice distortions within the porphyroclasts of each phase. In large orthoclase clasts, a continuous to heterogeneous misorientation pattern (**figure 8a**) evinces minor crystal-plasticity, with average misorientation values of 2° relative to the mean orientation, increasing to 17° towards clast rims, micro-fractures, and vein margins. Albite clasts display a similar misorientation pattern, with average misorientation values increasing towards the rims from 4° to 15°. The highest misorientation angles in the albite porphyroclasts (maximum of 73°) are localized near bent and fractured regions (**figure S5a**). Quartz porphyroclasts show a continuous misorientation pattern, with misorientations increasing from 0°-5° in the center of the grain to 5°-20° near HAGBs (**figure S6a**). The highest misorientation values (up to 46°) in quartz occur along irregular HAGBs and LAGBs towards the ultracataclastic veins. The HAGBs of fine-grained (<60 μm) albite, orthoclase and quartz adjacent to, and within, the ultracataclastic veins are irregular to smoothly curved. These grains contain a paucity of LAGBs and have low (~0-8°) internal misorientations relative to the mean, indicative of low internal strain. Few instances of albite and pericline twinning are observed in the fine-grained albite fragments of the host rock (**figure S4a**).

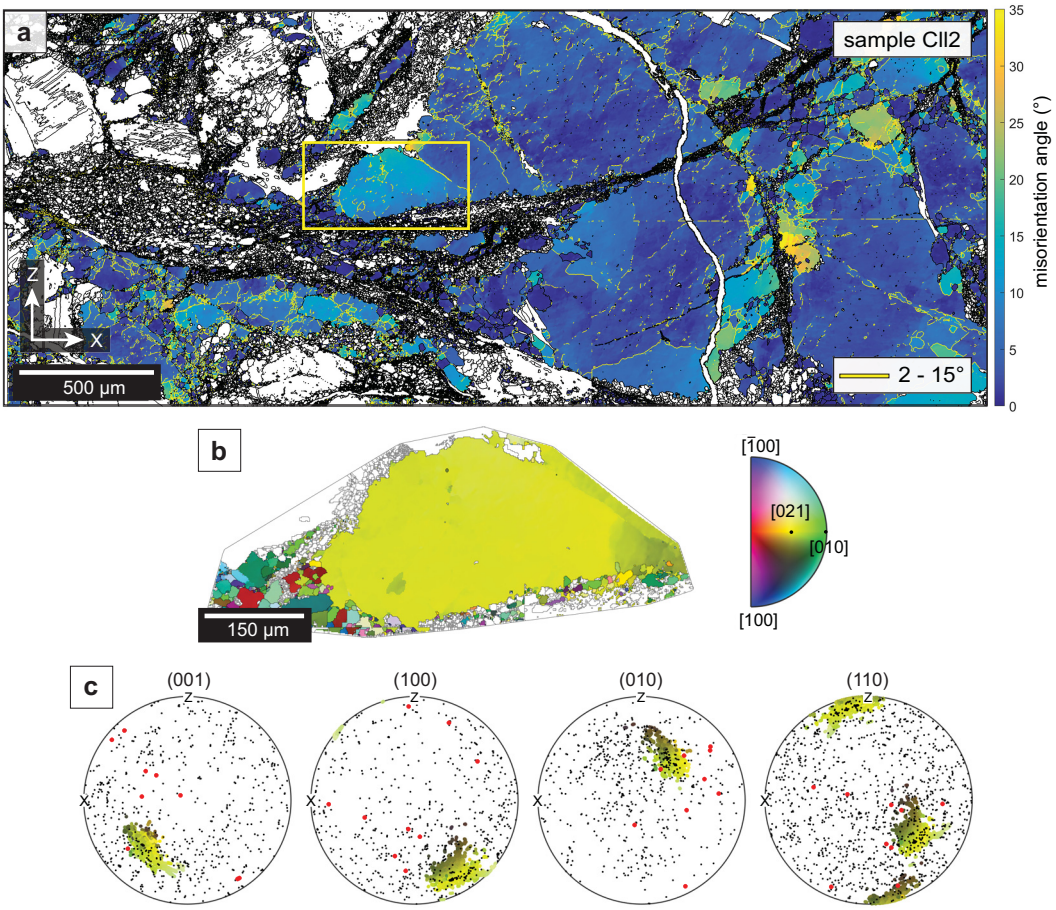

Figure 8. Grain orientation analysis on orthoclase populations in sample Cll2. (**a**) Orientation deviation angle map of orthoclase showing misorientation relative to grain average orientation, and LAGBs outlined in yellow. The map evinces minor crystal plasticity in the form of a continuous to heterogeneous misorientation pattern within the larger grains. Higher misorientations occur along the rims and in the vicinity of micro-fractures (maximum misorientation of 52°). Relatively no misorientations are present within the smaller grains. Yellow box shows pole figure subset area displayed in b. (**b**) IPF-Y map of orthoclase grains in the analysis subset and corresponding IPF key for orthoclase. (**c**) Lower hemisphere pole figure showing the IPF-Y orientation spread of pixels in the large orthoclase host clast (2.0 mm), relative to the mean orientation of the small orthoclase grains (<40 µm) surrounding the clast (black markers, one point per grain). The mean orientation of albite grains surrounding the large clast are plotted in red (one point per grain).

In the inverse pole figure (IPF) map for sample Cll2 (**figure S7a**), the large orthoclase clast and the fragments surrounding the large clast are similarly oriented (between [021] and [010]), suggesting minimal rotation of the fragments relative to the porphyroclast. Whereas the albite porphyroclasts within the host rock and vein matrix of Cll2 exhibit a random distribution of crystal orientations (**figure S7b**). Fragments of each phase closest to the vein margin also show a wider distribution of orientations. The orientations of larger porphyroclasts were plotted relative to the orientations of surrounding fine grains of the same phase at the margins of the veins (**figure 8**: orthoclase; **figure S5**: albite; **figure S6**: quartz). The resultant pole figures for each phase subset show scattered orientations with no defined maxima in the small grains relative to the host clast. Pole figures of the quartz porphyroclasts in map Bp6 (**figure S7c, d**) display a crystallographic preferred orientation, with c-axis maxima concentrating around [Y] (perpendicular to lineation). Both the a- $\{11\bar{2}0\}$ and m- $\{10\bar{1}0\}$ axis orientations form maxima distributed along the periphery of the pole figures. In the corresponding misorientation axis distribution plot (**figure S7e**), the quartz misorientation axes mostly concentrate around the c-axis.

5.1.2 Ultracataclastic veins

Due to the fine-grained nature of the ultracataclastic veins, many pixels in the EBSD maps were either misindexed or could not be indexed at all, limiting our ability to properly analyze grain shapes, sizes, and orientations. This is likely a result of the grain size being smaller than the step size used for EBSD analysis (1.25- 2.5 μm), which prevents distinguishing between fine fragments and amorphous material. However, based on the limited grains that did index reasonably well, grain shapes within ultracataclastic veins vary between the EBSD maps. In the vein of sample Dp3 there are sub-angular grains of both albite and quartz up to 113 μm wide (**figure S4b**). In contrast,

the ultracataclastic grains in sample Cll2 are dominantly albite and appear rounded and equant, with a maximum diameter of 71 μm (**figure 7b**). The albite fragments in this vein are likely derived from the fractured albite clasts directly adjacent to the vein. Similar trends are observed in EBSD maps of sample Bp4 and Bp6 (**figure 7a; S4a**), where fragments within the veins are primarily the same phase as the nearest porphyroclast bordering the vein margin. Misorientation and IPF maps show that the fine-grained populations of albite, orthoclase, and quartz within the ultracataclastic veins are randomly oriented, with no systematic misorientation relationships to the larger porphyroclasts neighboring the veins. Grains within the veins have low (<5°) internal misorientations near grain boundaries, whereas several larger clasts display higher internal misorientations of up to 12° along grain boundaries. LAGBs are infrequent in the vein material and concentrated towards the rims of larger clasts (~20-115 μm).

5.2 Geochemical results

To assess potential correlations between the observed microstructures and compositional heterogeneities within the various phases, we conducted a series of geochemical investigations on the same samples (All, Bp, Cll, Dp) that were analyzed via EBSD methods. Chemical variations within the feldspar porphyroclasts are evident as greyscale contrasts in BSE images. Analysis of BSE images from sample Cll2 (**figure 9a**) reveals a generally homogeneous orthoclase composition, with pores ubiquitously distributed. The highest density of pores occurs near micro-fractures within the orthoclase porphyroclasts. Along the margins of fractures propagating from the tip of the ultracataclastic vein, fine-grained albite (<10 μm in diameter) forms a cuspate-lobate phase boundary with the surrounding orthoclase, extending up to 25 μm from the fracture (**figure 9a, b**). This cuspate-lobate boundary between albite and orthoclase is also observed in the petrographic photomicrographs (**figure 6d**). In BSE images, the albite grains are irregularly shaped

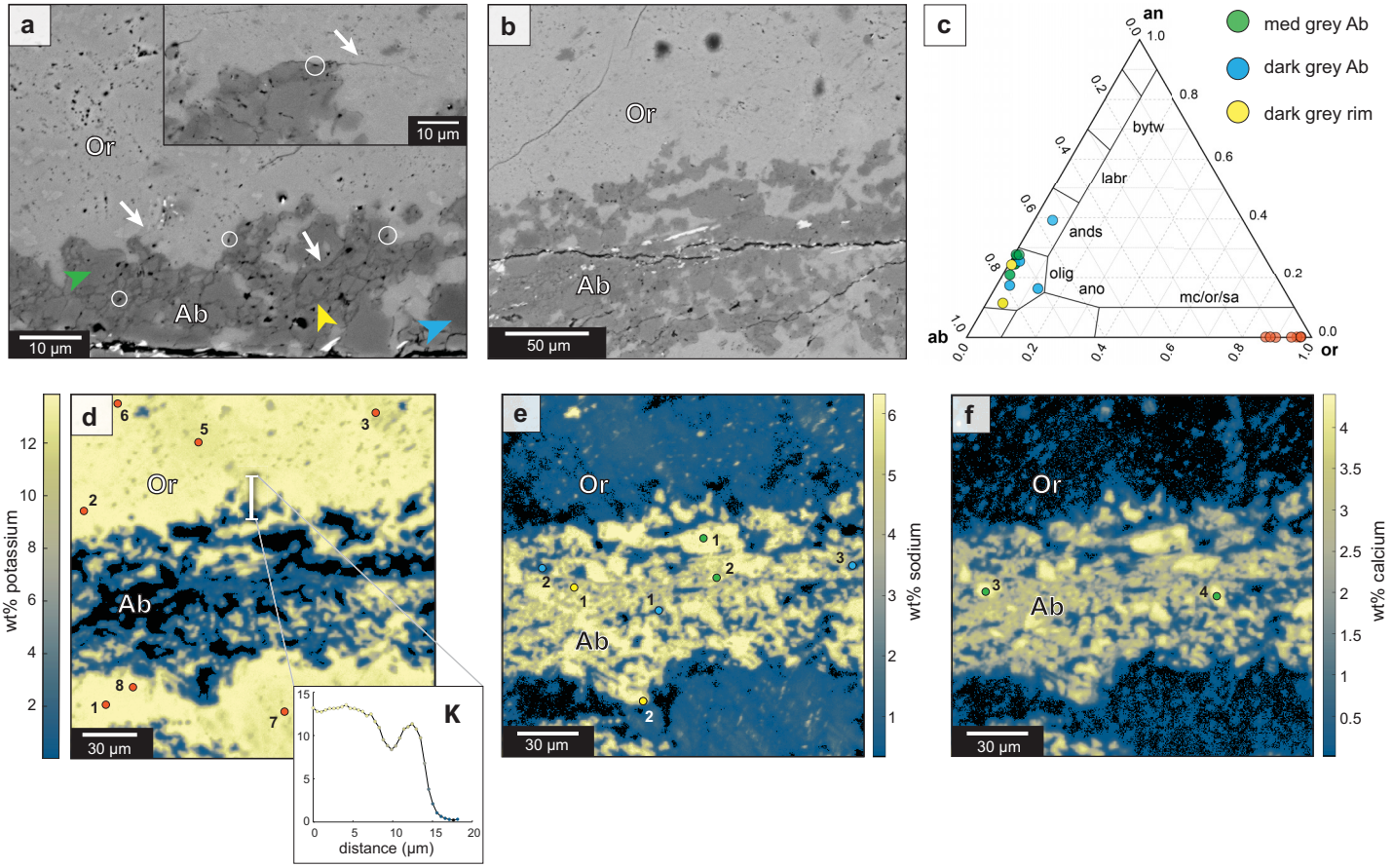

Figure 9. (**a**) BSE image of ultracataclastic vein margin in sample Cll2 showing possible dissolution reprecipitation reaction front. The orthoclase (Or) porphyroclast shows a cuspate boundary with fine-grained albite (Ab) aggregates (<45 µm) lining the vein margin. White arrows point to cracks along the phase interface, pores within albite and orthoclase along the boundary are circled in white. Three albite generations are noted by the colored arrows: the medium grey albite (green), the dark grey albite (blue), and the porous dark grey rim (yellow). Inset: a BSE image taken along the same vein margin in higher resolution of fracturing and porosity development at the phase interface. (**b**) BSE image of the cuspate phase boundary at the ultracataclastic vein margin in sample Cll2 and the EMPA X-ray map area shown in d-f. (**c**) Calculated albite and orthoclase compositions from EMPA analyses plotted onto the feldspar ternary diagram, with the three albite generations showing a range in compositions. (**d**) EMPA X-ray map for potassium, displaying compositional variations in the feldspars near the orthoclase-albite boundary. Orthoclase porphyroclast rims are depleted in potassium. The sampled transect across the interface shows a step function decrease in potassium. Orthoclase spot analyses are shown as numbered orange circles. The corresponding wt% values of each analysis are listed in table S2. (**e-f**) EMPA X-ray maps for sodium and calcium, with albite spot analyses colored according to the generation (table S2).

and display varying greyscale contrasts, from medium to dark grey (**figure 9a**). A dark grey, porous albite generation forms a thin rim (1-4 μm) around the medium to dark grey grains. In general, pores in the albite are located at grain boundaries and triple junctions. Pores appear more frequently within the medium grey albite grains. Micro-cracks are commonly observed along albite grain boundaries near the phase interface and are associated with increased pore concentrations. Within the orthoclase inclusions of albite occur near pores, extending up to 70 μm from the phase boundary. The fractures in the orthoclase clasts terminate at the orthoclase-albite phase boundaries. The orientations of albite grains and a large orthoclase clast at the phase boundary are plotted on pole figures in **figure 8c**. The random distribution of albite grain orientations relative to the orthoclase demonstrates that there is no obvious crystallographic relationship between the phases.

Electron microprobe chemical mapping across the orthoclase-albite confirms compositional variations within both phases. Points selected on the chemical maps reveal a normalized orthoclase composition of $Or_{88\text{-}97}$ $Ab_{03\text{-}11}$ $An_{0.1}$ (**table S2; figure 9c**). Near micro-fractures, pores and albite inclusions in the orthoclase, potassium concentrations locally decrease by ~3.7 wt% and sodium concentrations increase to 3.6 wt% (**figure 9d, e**). At the orthoclase-albite interface, a marked ~3 μm wide potassium-depleted and sodium-enriched margin is observed within the orthoclase along the phase boundary, with potassium concentrations decreasing from ~13.6 wt% to 9.5 wt%, whereas sodium increases from 0.4 wt% to 1.7 wt%. Points selected from the albite grains reveal a composition of $Ab_{71\text{-}73}$ $An_{20\text{-}26}$ $Or_{05\text{-}1.4}$ (**table S2**; **figure 9c**). Although the proportions of sodium and calcium remain similar between the medium and dark grey albite grains, the latter consistently possesses higher silica content (42.0 wt% vs. 28.0 wt% in the medium grey phase) and is depleted in sodium, calcium and aluminum (1.5 wt% Na, 0.8 wt% Ca, 3.3 wt% Al, compared to 6.5 wt% Na, 4.1 wt% Ca and 13.0 wt% Al). As a result, relative variations in sodium

and calcium appear pronounced when plotted on the ternary diagram, resulting in a broader distribution of points (blue in **figure 9c**). Notably, the silica and aluminum concentrations in the medium grey albite grains are complementary to those in the adjacent orthoclase (~30 wt% SiO_2 and 10 wt% Al). Potassium concentrations in the dark grey albite grains also vary more widely across individual analytical spots (0.1-0.4 wt% K), whereas the medium grey albite values are uniformly ~0.2 wt% K. A precise composition of the porous dark grey albite rim could not be reliably obtained from spot analyses, reflected in the slight data dispersion on the ternary diagram (yellow in **figure 9c**), where points vary from 1.5-3.1 wt% in calcium.

6. Discussion

The design of this study was to investigate the nucleation and propagation mechanisms of a series of ultracataclastic veins within the high-strain zone of the Naxos granodiorite, through comprehensive outcrop observations and 2D microstructural analyses. Complementary electron microprobe geochemical analyses were performed on phases along the vein margin to assess the possible chemical changes that have resulted from deformation along rupture paths. The ultracataclastic material is fine-grained (<2 mm), and of the same composition as the host rock, consisting primarily of albite, orthoclase, and quartz fragments. Microstructural analysis reveals that the vein material does not preserve ductile structures and instead appears to be dominantly associated with brittle fracturing and cataclasis. Herein, we discuss the processes governing ultracataclastic vein genesis and the potential interplay between rupture, brittle deformation, and potential fluid-mediated reactions.

6.1 Deformation of the granodiorite prior to vein emplacement

To differentiate between microstructures in the host rock that predate the emplacement of ultracataclastic veins and those that result from it, we compare microstructures preserved in the strain zone 0 granodiorite with those from zone 5. In the sample from zone 0, quartz grains evince minor dynamic recrystallization via subgrain rotation, as shown by irregular grain boundaries, undulose extinction and subgrain development towards clast rims, with adjacent grains the same size as the subgrains (**figure 6a**; Stipp et al., 2002). The presence of subgrain rotation recrystallization structures provides an estimate of deformation temperatures prior to cataclasis between ~400°C and ~510°C (Stipp et al., 2002). Quartz porphyroclasts in the zone 0 sample are larger (0.1-2 mm) and more equant than the quartz grains in the zone 5 samples (0.4-1 mm). The zone 5 quartz porphyroclasts away from the ultracataclastic veins show irregular or amoeboid grain shapes, abundant subgrains, and interfingering grain boundaries, characteristic of extensive recrystallization via subgrain rotation and grain boundary migration (**figure 6b**; Stipp et al., 2002). These features support dynamic recrystallization as the primary mechanism for grain size reduction in quartz during crystal-plastic deformation, consistent with the conclusions of Bessiere et al. (2018), who documented progressive quartz grain size reduction via recrystallization in the granodiorite towards the detachment plane.

The recrystallization of quartz and resulting shape preferred orientation in the zone 5 samples are indicative of strain accommodation by dislocation creep in the crystal-plastic regime (Hirth & Tullis, 1992; Stipp et al., 2002). Further, the presence of both grain boundary migration and subgrain rotation recrystallization places the upper limit of possible deformation temperatures to ~600°C (Stipp et al., 2002). The c-axis pole figure for the quartz porphyroclasts shows a central maximum perpendicular to lineation, whereas the a- and m-axis pole figures display periphery

maxima (**figure S7d**). This CPO pattern in the quartz pole figures corresponds with dominant prism <a> slip, which occurs at temperatures of 500-550°C (Schmid & Casey, 1986; Barth et al., 2010; Zuo et al., 2021). The quartz misorientation axes are concentrated in the c-axis ({0001}) of the axes distribution plot (**figure S7e**), which is also characteristic of a prism <a> slip system (Neumann, 2000; Zuo et al., 2021). These deformation temperature estimates align with previous studies of the granodiorite, such as Bessiere et al. (2018), which reported a range across temperatures of 450-550°C that were determined from quartz crystallographic preferred orientations in high strain shear bands. Similarly, Cao et al. (2017) estimated deformation temperatures for a granodiorite sample in zone 2 between 583°C and 661°C, calculated using the hornblende-plagioclase geothermometer (Holland & Blundy, 1994). The estimated temperature range is also consistent with the generalized temperature-time path of the Naxos granodiorite emplacement originally inferred by Gautier et al. (1993).

In this temperature range, albite and orthoclase accommodate deformation by internal micro-cracking (Tullis & Yund, 1992). This behavior is consistent with microstructures observed in the low-strain granodiorite sample (**figure 6a**), where albite and orthoclase porphyroclasts display fracturing, patchy extinction, and minor subgrain development, particularly near clast rims. Feldspar porphyroclasts in zone 5 exhibit many of the same deformation structures as those in zone 0, but with greater intensity. These structures include irregular grain shapes, patchy extinction and increasing micro-crack formation towards clast rims, with localized concentrations of porosity (**figure 6c, d; 7**). The zone 5 feldspar microstructures evince dominantly brittle deformation mechanisms, accommodated by minor crystal-plasticity via dislocation glide and climb (Fitz Gerald et al., 1991; McLaren & Pryer, 2001). Therefore, although brittle microstructures in the high strain zone are probably associated with coseismic slip and ultracataclasis (discussed below),

some fracturing and lattice distortions in the feldspars likely formed earlier. Based on these microstructural observations, deformation prior to vein emplacement occurred in the crystal-plastic regime of quartz (450-550°C), whereas deformation coeval to vein injection was dominated by cataclasis of feldspar and quartz.

6.2 Deformation of the granodiorite related to vein emplacement

From the microstructures observed in the photomicrographs, EBSD maps, and BSE images, it is evident that cataclasis is the primary deformation mechanism in areas surrounding the ultracataclastic veins. Fractures and apparent LAGBs in albite, orthoclase, and quartz porphyroclasts of the granodiorite are extensive and increase in density with proximity to the veins, as grain size decreases. As shown in the BSE images (**figure 7a inset**), most of the features documented as LAGBs in the feldspar porphyroclasts are instead intracrystalline micro-fractures. Porphyroclasts of all phases are angular, consistent with formation by brittle fracturing during rupture (Lloyd & Knipe, 1992; Stünitz & Fitz Gerald, 1993; Petley-Ragan et al., 2018). The bookshelf micro-fracturing present in some of the feldspar porphyroclasts (**figure S3d**) includes rigid feldspar blocks without any boudin necks, rotated along discrete fractures, which suggests the structures were produced in the brittle regime (Pryer, 1993; Goscombe & Passchier, 2003; Moreira & Dias, 2018). The large fragments of albite and orthoclase porphyroclasts in samples Bp4 and Cll2 show minimal rigid rotation in EBSD IPF maps (**figure S7a**). However, considerable rotation of the smaller feldspar fragments neighboring these porphyroclasts is evinced by sub-angular to sub-rounded grain shapes and orientations in the IPF maps. Similar host rock damage zone characteristics are reported by Michalchuk et al. (2023) and Jefferies et al. (2006), where grain size reduction towards vein margins is facilitated by fracturing and rotation. In sample Cll2,

the fracture pattern of the large orthoclase porphyroclasts (**figure 7b**) aligns with the vein tip propagation model of Mancktelow et al. (2022), where fractures splay from the fault tip into the wall rock at oblique angles to the vein emplacement plane.

To determine whether small grains adjacent to the porphyroclasts were produced by cataclasis or dynamic recrystallization, the grain orientations were compared using IPF maps, grain orientation deviation maps, and pole figures. Subgrain rotation and grain boundary migration processes would result in continuous misorientation patterns in the strained parent grains, with misorientation values increasing toward subgrain boundaries and clast rims (Zuo et al., 2021). The surrounding recrystallized grain populations would exhibit a crystallographic preferred orientation relative to the orientation of the relict parent grain (Hobbs, 1968; Halfpenny et al., 2006). In our samples, pole figures of the mean orientations of fine grains relative to their bordering host clast of the same phase show random grain orientation distributions without any maxima (**figure 8c:** orthoclase; **figure S5c:** albite; **figure S6c:** quartz). The scattered orientations of the fine-grained populations are indicative of fragmentation via cataclasis. The straight to curved grain boundaries of the fine-grained populations neighboring the porphyroclasts further support this interpretation, as cataclastic fragments tend to show angular, rather than diffuse boundaries (Stünitz & Fitz Gerald, 1993).

EBSD grain orientation deviation maps (**figures 8a, S5a, S6a**) reveal continuous to heterogeneous misorientation patterns in the porphyroclasts, with lattice distortions concentrated towards the clast rims, apparent LAGBs, and fractures. The continuous misorientation patterns are suggestive of minor dislocation glide. Near vein margins, albite porphyroclasts with internal misorientation and undulose extinction possess bent twins curving towards the ultracataclastic veins (**figure 6c, 7a**). The bent twinning is also evidence for dislocation glide, which may have led

to strain hardening and micro-fracturing in the albite clasts (Hentschel et al., 2019). Many healed micro-fractures are often observed next to the bent twin boundaries, suggesting that fracturing and deformation twinning in the albite are complementary. Other studies, such as Jefferies et al. (2006) and Menegon et al. (2017), have also documented deformation twinning proximal to ultracataclastic and pseudotachylytic vein margins.

The micro-fractures, deformation twinning, and patchy extinction in the feldspar porphyroclasts are consistent with the experimental findings of Tullis and Yund (1987) on feldspar deformation in the cataclastic flow regime. Their study, using transmission electron microscopy imaging, revealed that microstructures such as apparent patchy undulatory extinction and subgrain development resulted from micro-fracture arrays rather than low-temperature plasticity. This is supported by experimental studies such as Fitz Gerald et al. (1991), who observed undulatory extinction and dislocation structures within micro-crack ladders, showing that host crystals can accommodate brittle fracturing through narrow zones of plasticity. Additional studies (McLaren & Pryer, 2001; Cervellon et al., 2020) report generation of dislocations from intragranular fracturing, a process also documented in pyrite (Rogowitz et al., 2018) and garnet (Dubosq et al., 2024) in the semi-brittle regime. The presence of these microstructures near the ultracataclastic veins demonstrate that the feldspar and quartz porphyroclasts accommodated strain through a combination of brittle fracturing and localized crystal-plasticity, reinforcing the model of cataclasis as the dominant deformation mechanism during vein emplacement.

6.3 Emplacement of ultracataclastic veins

Pseudotachylytes and ultracataclasites are cohesive fault rocks that develop along localized rupture paths during coseismic slip (Sibson, 1977). Pseudotachylytes are glassy quenched melts

produced from frictional heating along the slip surface (Philpotts, 1964; Sibson, 1975), whereas ultracataclasites, characterized by matrix proportions of 90%-100% (Sibson, 1977), form through the comminution of host rock by continued micro-fracturing, grain sliding, and rotation, leading to significant grain size reduction (Sibson, 1977; Onasch et al., 2010). It remains difficult to differentiate between pseudotachylytes and ultracataclasites in the field, particularly as these structures are susceptible to reworking or alteration. Key indicators of frictional melting include microlites, flow structures, sharp contacts with the host rock, concoidal fractures, and vesicles, among others (Sibson, 1975; Lin, 1994; Kirkpatrick & Rowe, 2013; Zhang et al., 2021). In ultracataclasites, post-pulverization processes such as thermal pressurization and fluidization promote rapid injection of the comminuted fine-grained material into surrounding coseismic fractures producing vein networks (Lin, 1996; Rowe et al., 2005; Ujiie et al., 2007a; Lin, 2019). Similarly, thermal expansion and pressurization can lead to triangular-shaped offshoots and veinlets of pseudotachylytic material from the main slip surface, referred to as injection veins (Rowe et al., 2012). In subsequent coseismic slip events, rupture paths will exploit pre-existing mechanically weak zones, such as pre-existing fault planes and fractures (Hodge et al., 2018). This can lead to reworking of vein material and further propagation along fractures (Chester & Chester, 1998). Many field studies have documented the co-occurrence of these fault rocks, for example along the Tonale fault (Pennacchioni et al., 2006), the Shimanto accretionary complex (Ujiie et al., 2007a), and the Kings Canyon faults (Kirkpatrick & Shipton, 2009). Spray (1995) concluded that comminution can act as a precursor for pseudotachylyte formation, providing the fine-grained groundmass for frictional melting.

Formation of pseudotachylytes, ultracataclastic veins, and cataclastic zones represents the transition from the ductile to brittle deformational regime associated with movement along the

extensional NPDS (John & Howard, 1995; Bessiere et al., 2018). In outcrops along the Stelida Peninsula, the ultracataclastic veins locally contain zones of glassy black material, which might be pseudotachylytic material (i.e., **figure S3a**), suggesting that narrow regions of the fault rock may have experienced frictional heating during slip. Further microstructural analyses, such as transmission electron microscopy, would assist in distinguishing this material from the ultracataclasites. The foliation-parallel pseudotachylytes and ultracataclastic veins preserve sharp contacts with the surrounding host rock, implying that the vein material was emplaced through rapid injection (Lin, 1996). This is also supported by the overall homogeneous composition of the veins, as relatively slower flow of pulverized grains into fractures would lead to sorting of the fragments (Ujiie et al., 2007a; Lin et al., 2013). Across the meter-scale to micrometer-scale, the injection of cataclastic material locally overprints earlier ductile deformation structures, as evinced by the lack of defined shape preferred orientations in quartz in the damage zones surrounding the veins. However, the apparent crenulation cleavage visible in some of the veins (**figure 6f**) indicates that the veins were emplaced syntectonically, developing a microstructure due to later folding. Injection veins at the outcrops (**figure 4b**) and in thin sections (**figure S3e**) commonly bend into the tectonic foliation, providing additional evidence for sustained deformation following vein emplacement.

At the vein tips, the ultracataclastic material appears to be derived directly from neighboring porphyroclasts as illustrated in photomicrographs, BSE images, and EBSD maps (**figure 6c, d; 7**). The vein margins are gradational, with a damage zone of fragments produced from comminution increasing in grain size towards the host rock porphyroclasts, as shown in sample Bp4 (**figure 7a**). The ultracataclastic vein material exhibits some degree of microstructural maturation from progressive grain size reduction and abrasion associated with injection, indicated

by material that is pervasively fine-grained and subrounded. Yet, the presence of angular fragments and larger clasts within the veins suggest a multi-stage vein evolution process. This heterogeneity in clast shapes may indicate that older clasts have rotated and become rounded through continued cataclastic flow, whereas newly generated clasts retained their angular shape (Sibson, 1975). These new fragments are likely incorporated into the vein material, and transported along fractures exploited by rupture paths produced during subsequent coseismic slip events. At Cape Achapsi, in the cataclastic zone below the NPDS, examples of multiple generations of ultracataclasis are observed in thin section (**figure 6e**). Older veinlets are preserved in clasts within a newer encompassing vein. At Stelida, ultracataclasis is restricted to discrete rupture paths, with limited overprinting of the host rock matrix by cataclasis away from the veins. Here, we interpret the thickest veins parallel to the foliation to be major rupture paths where cataclastic material is reworked and transported along the same planes. The crosscutting relationships observed in the field between foliation parallel veins and veins steeper than foliation (**figure 3b, 4c**) further demonstrate a multi-event history of vein formation and propagation.

6.4 Origin of albite aggregates

The fine-grained albite populations (<10 μm) neighboring the orthoclase porphyroclasts at the vein boundary in sample Cll2 (**figure 7b**) could be a product of various processes, including (1) fragmentation associated with rupture, (2) neocrystallization of albite, or (3) dissolution-reprecipitation from the adjacent orthoclase clasts.

1) The albite grains may result from the comminution of nearby albite porphyroclasts during cataclasis, with fragments transported into the fractures during vein injection. In the EBSD phase map for sample Cll2 (**figure 7b**), many of the small albite grains within the damage zone

appear to originate from the adjacent fractured albite porphyroclasts. Yet, grains adjacent to the orthoclase have irregular to curved grain boundaries, rather than the straight boundaries characteristic of breakdown via micro-fracturing and rotation (Lloyd & Knipe, 1992). Injection of the small grains alone would not account for the lobate phase boundary and albite inclusions observed along the orthoclase clasts.

2) Heterogeneous nucleation, or neocrystallization, of albite can occur as a product of metamorphic reactions or precipitate from pore fluids, with the phase nucleating along defects such as dislocations, grain boundaries, or inclusions (Fitz Gerald & Stünitz, 1993; Stünitz, 1998). This process is driven by compositional disequilibrium rather than mechanical fragmentation, resulting in chemically distinct grains that do not have a crystallographic relationship to the original potassium feldspar (Hentschel et al., 2019). This is consistent with our EBSD results, as pole figures of albite grain orientations relative to the bordering orthoclase clast display a random distribution (red points in **figure 8c**), indicating that there is no crystallographic relationship between the feldspars across the phase boundary.

3) Fluid-mediated replacement of potassium feldspar by albite can occur through an interface-coupled dissolution-reprecipitation mechanism, by the following reaction (Putnis, 2009; Norberg et al., 2011; Hentschel et al., 2019):

$$KAlSi_3O_{8\,(solid)} + Na^+_{(aq)} \leftrightarrow NaAlSi_3O_{8\,(solid)} + K^+_{(aq)} \quad (1)$$

Such replacement processes are driven by solubility differences between the parent and the product phases in the presence of a fluid, which induces dissolution of orthoclase. In this reaction, the neoblastic albite would have the lowest solubility in the fluid, and preferentially precipitate over orthoclase (Hövelmann et al., 2010). Key microstructures associated with this reaction include a sharp reaction interface and cuspate grain boundaries between the parent and product grains

(Norberg et al., 2011), both of which are present in our samples. EMPA transects across the interface (**figures 9d; S9c, d**) show abrupt elemental transitions between the albite and orthoclase phases over a narrow 1-3 μm wide zone. In BSE images of the ultracataclastic vein margin in sample Cll2, the lobate phase boundary between the orthoclase porphyroclasts and protruding albite aggregates is prominent (**figure 9a**). The presence of these features suggests that the fine grains of albite neighboring the orthoclase clasts are precipitates, rather than cataclastic fragments, formed from dissolution-reprecipitation. Although albite was produced at the reaction front, aqueous potassium must have been transported and precipitated elsewhere in the system as new biotite or orthoclase grains (Hentschel et al., 2019). As ultracataclastic vein emplacement is related to the semi-brittle deformational regime and has been dated at c. 9.9 Ma by Andriessen et al. (1979), the fluids facilitating this reaction at the vein tips are likely meteoric in origin, percolating from the upper brittle crust (Siebenaller et al., 2013; Cao et al., 2017). Alternatively, these fluids may have originated from upper crustal, low-grade metamorphism, or represent a mixture of both fluid sources, based on the conceptual model for fluid circulations within the Naxos metamorphic core complex across the brittle-ductile transition (Siebenaller et al., 2013).

The interface-coupled reaction process results in a compositionally distinct albite phase that retains the original grain morphology across the reaction interface (Putnis, 2009; Hövelmann et al., 2010; Norberg et al., 2011). The crystallographic information of the initial orthoclase structure is transferred to the product phase, creating a topotactical relationship where the newly formed albite occupies the original volume of the orthoclase grain (Plümper & Putnis, 2009). Therefore, the product grains should exhibit a crystallographic relationship to the adjacent orthoclase in EBSD mapping. However, the albite grains in our samples have random orientations, most likely due to rotation from multiple pulses of cataclasis. The compositional variations of the

product albite grains observed in EMPA elemental maps and BSE images suggest numerous episodes of nucleation and growth. The range of albite grain boundaries, from irregular to smoothly curved, is further indicative of differing degrees of rotation and textural maturity.

To sustain fluid access to the reaction front and facilitate replacement, intracrystalline porosity and permeability is developed within the product phase (Putnis & Austrheim, 2010). In BSE images of the reaction front, generations of albite with differing porosities have been identified. These include a medium grey phase, a dark grey phase, and a dark grey porous rim along the other albite generations (**figure 9a**). The medium grey grains appear more porous than the dark grey grains, with increased pore concentrations along grain boundaries, triple junctions, and fractures along the reaction interface. The heterogeneous distribution of pores and porous rim observed within the albite aggregates further establishes formation via an interface-coupled reaction, as the permeability evolves alongside neoblastite formation to maintain contact with the reaction front (Putnis, 2009). Chemical maps indicate that the variation in BSE contrast between the two albite generations may result from nanoscale variability of potassium, sodium, calcium, aluminum, and silica concentrations (**figure 9d, f; S8, S9**). The consistently higher silica and lower aluminum concentrations in the dark grey albite grains may be due to a change in the composition of the fluid source driving the interface coupled reaction. Alternatively, this trend may be related to Si/Al disorder in the newly formed grains following the complete breakdown of the orthoclase structure (Norberg et al., 2011), suggesting that these grains represent a later generation which did not reach equilibrium. The Si/Al compositional variation between the two albite generations may also reflect the leaching of mobile elements from the dark grey grains at a point in the evolution of the reaction front. Overall, the presence of multiple generations of compositionally distinct albite phases reflects multiple episodes of fluid influx and dissolution reprecipitation. At the

outcrop scale, fluid flow is documented by the bleached zones of host rock adjacent to the foliation-parallel veins (section 3.1), the abundant biotite within and surrounding the veins, as well as the pervasive chloritization near the detachment, particularly at the Galini and Cape Achapsi sites. These observations reinforce a multi-stage and sustained history of fluid movement through the granodiorite below the NPDS, establishing the conditions required for the interface-coupled replacement reactions noted at the grain scale.

In laboratory experiments, progression of interface-coupled reactions has been shown to induce micro-fracturing in potassium feldspar along the reaction front (Putnis et al., 2009; Norberg et al., 2011). The interface is semi-coherent, and a slight misfit between the lattices of orthoclase and albite produce elastic strain, leading to micro-fracturing. This is observed in BSE images of this study where many micro-fractures are present along the albite grain boundaries and extend into the orthoclase porphyroclasts (**figure 9a**). The EBSD phase map for sample Cll2 also shows apparent LAGBs propagating from the reaction front into the orthoclase (**figure 7b**). The associated EBSD grain orientation deviation map reveals increasing misorientation angles towards the reaction front (**figure 8a**). Although this pattern is likely driven by plastic strain associated with vein injection, the production of elastic strain during dissolution-reprecipitation may have also contributed to the localized concentrations of lattice distortions at the orthoclase clast boundary. Scanning transmission electron microscopy or high-resolution EBSD would need to be employed to verify the origin of the lattice distortions at the clast boundaries. In BSE images and EMPA maps of the orthoclase porphyroclasts (**figures 9; S8)**, sodium-enriched regions, albite inclusions and pores are spatially associated with fractures, indicating that fluid movement exploited these pathways during replacement. Therefore, initial fractures in the orthoclase porphyroclasts from cataclasis facilitated fluid infiltration, and the ensuing dissolution-

reprecipitation lead to further micro-cracking and porosity development. This process produces a more permeable orthoclase phase at the reaction front. Ultimately, the combined dissolution of orthoclase and precipitation of porous albite neoblastites contributed to localized weakening along the ultracataclastic vein margins.

6.5 Feedback between cataclasis and dissolution-reprecipitation

With our new field observations, microstructural analyses, and geochemical mapping of feldspars from ultracataclastic veins in the high strain zone of the Naxos granodiorite, we propose a model of repeated rupture events driven by chemo-mechanical processes. Cross-cutting relationships between foliation-parallel ultracataclastic veins and veins steeper than foliation establish a multi-generational vein emplacement history (**figure 3, 4c**). Samples from Cape Achapsi display older generations of veinlets preserved within clasts of a more recent ultracataclastic vein (**figure 6e**). Further, the presence of both angular and rounded fragments in the ultracataclastic veins attests to an evolution of microstructural maturity, consistent with repeated comminution of the host rock. These observations demonstrate that ultracataclastic processes on Naxos were episodic, with each subsequent rupture event increasing fracture networks and contributing to cataclasis of the host rock.

Fluidization of the comminuted material likely occurred due to thermal pressurization during coseismic slip and cataclasis (Lin, 1996; Rowe et al., 2005). Pressure gradients generated by dilatancy associated with ultracataclasite propagation would have induced fluid flow to the densely fractured areas surrounding the veins (Jefferies et al., 2006; Lin, 2019). In the presence of the infiltrating fluids, orthoclase porphyroclasts along the vein margin underwent dissolution driven by chemical disequilibrium with the fluid phase (Putnis, 2009). This was followed by the interface-coupled precipitation of albite, producing fine-grained albite at the vein tip.

Compositional variations in the neoblastic albite compositions, observed in EMPA maps and BSE images, indicate multiple pulses of fluid influx and dissolution-reprecipitation occurred along the vein margins.

We propose that after cataclasis, the interface-coupled reactions generated a feedback loop that promoted subsequent fracture propagation and sustained injection of ultracataclastic material within the granodiorite (**figure 10**). During ensuing coseismic events, the orthoclase porphyroclasts, weakened by increased porosity and fracturing from the reaction, would be more susceptible to pulverization. Experimental results from Bons and Jessell (1999) conclude that anastomosing micro-shearing preferentially localizes along grain boundaries in fine-grained material. Thus, the newly formed albite grains act as weaker zones that can be exploited by subsequent rupture pathways. The neoblastic albite is also highly porous, with micro-cracks along grain boundaries that can propagate and link during rupture, allowing preferential vein migration through these zones. As a result, the fractured orthoclase and new albite grains become incorporated into the comminuted material within the evolving vein. Recent deformation experiments at eclogite facies conditions by Soret et al. (2025) further demonstrate the effectiveness of dissolution-reprecipitation creep in localizing strain, highlighting fluid-mediated processes that can promote weakening within crustal-scale shear zones.

Although pseudotachylytes have been shown to form and quench rapidly during seismic events, through both laboratory experiments (e.g., Conrad et al., 2023) and field observations (e.g., Sibson, 1975; Ujiie et al., 2007b; Bestmann et al., 2012, 2016), the duration of ultracataclastic flow related to coseismic slip remains uncertain (Corwin et al., 2005; Rowe et al., 2015). Experimental studies (i.e., Labotka et al., 2004, Hövelmann et al., 2010) on feldspar replacement in the presence of a fluid phase demonstrate that the dissolution-reprecipitation process can occur relatively

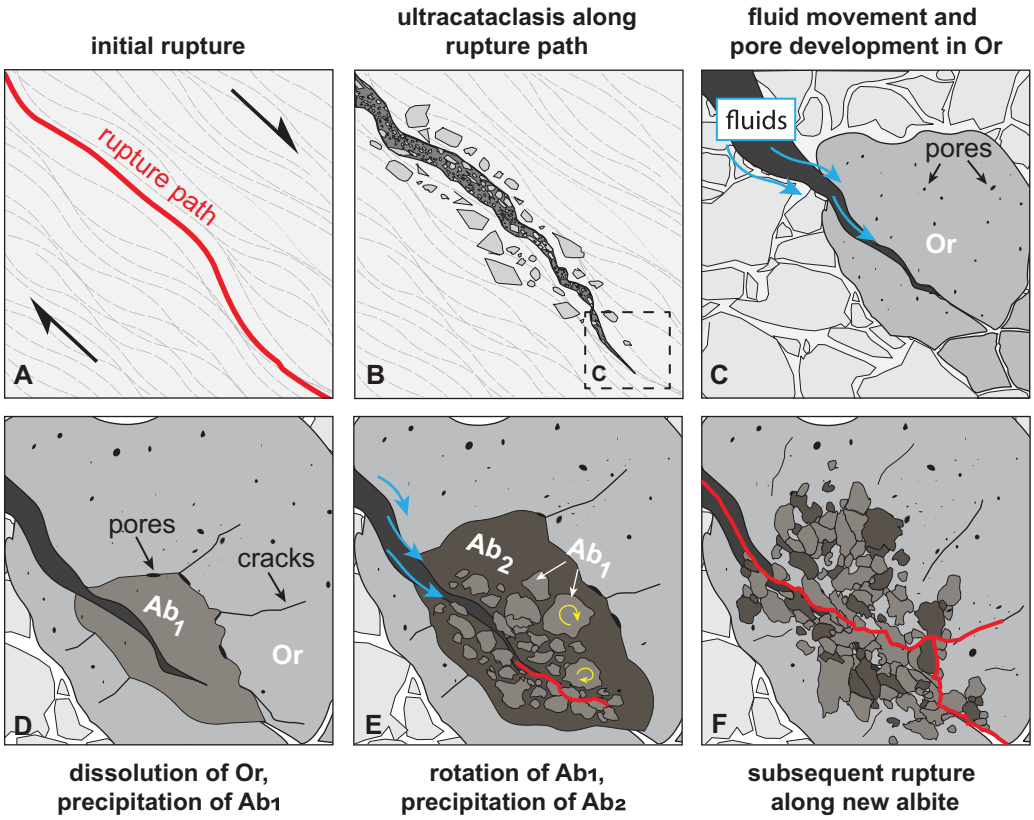

Figure 10. Schematic illustration of ultracataclastic vein emplacement and successive dissolution-reprecipitation reactions along the vein margin from fluid mobility. Box **A** shows a rupture path through the tectonically foliated granodiorite proximal to the NPDS. Box **B** shows fragmentation and ultracataclasites injected along the path, terminating at a vein tip. In box **C** fluids are mobilized during injection (blue arrows) and travel along the vein producing localized zones of weakness by facilitating porosity development in orthoclase porphyroclasts. In box **D** orthoclase is replaced by albite through a dissolution-reprecipitation reaction, producing pores along the new albite (Ab_1)-orthoclase phase boundary and cracks in the orthoclase. Box **E** shows fragmentation and rotation of Ab_1 from a subsequent rupture (red) and the precipitation of a second albite generation (Ab_2) with continued fluid movement (blue arrows). In box **F** a rupture path preferentially travels along the fine-grained neoblastic albite and new fractures.

quickly, in a matter of days or weeks at typical hydrothermal conditions (Plümper & Putnis, 2009; Putnis, 2009). However, the reaction rate is controlled by (1) the rate of fluid transport to the reaction front, and (2) the supersaturation and chemistry of the infiltrating fluid (Putnis, 2009). In natural systems, the albitization of orthoclase likely proceeds more slowly than seismic slip and the initial injection of ultracataclastic veins, which transpires in seconds to minutes (Sibson, 1975; Swanson, 1992). Therefore, the proposed feedback loop model is considered to occur through reactivation of the rupture path in subsequent coseismic slip events, rather than contributing to vein propagation during the initial slip and vein injection. This cyclic process of rupture, fluid infiltration, and mineral replacement highlights the interplay between mechanical and chemical weakening along the rupture path, ultimately influencing the long-term evolution of fault zone architecture.

7. Conclusions

We have characterized three types of ultracataclastic vein sets in the high-strain zone of the Naxos granodiorite subjacent to a major crustal-scale detachment fault, including foliation-(sub)parallel veins, veins steeper than foliation, and veins striking oblique to foliation, which display crosscutting relationships. Our field observations provide a reinterpretation of outcrops long-cited as classic examples of pseudotachylytes. Microstructural analyses offer new insight to the origin of these fault rocks, supporting their re-classification. EBSD mapping at the foliation-parallel vein tips reveal dominantly brittle microstructures, confirming that cataclasis was the primary deformation mechanism related to vein propagation. This is reinforced by the spatial relationship between lattice distortions and micro-fractures in feldspar porphyroclasts, which suggests that the local accommodation of strain by crystal-plasticity was linked to brittle

deformation. The range in grain shape and size within the ultracataclastic veins – from larger angular clasts (up to 97 μm) to homogeneous rounded clasts (5-70 μm) – reflects variations in structural maturity of the vein material. The combined field, petrographic, and microstructural observations demonstrate an episodic history of coseismic slip and vein emplacement, where host rock porphyroclasts underwent repeated fragmentation, rotation, and injection along rupture paths.

At the vein tips, a cuspate phase boundary between large orthoclase porphyroclasts and albite aggregates is indicative of an interface-coupled dissolution-reprecipitation reaction front. Progression of the reaction led to fracturing and porosity development within the relict orthoclase, weakening the porphyroclasts. The neoblastic albite is fine-grained (<10 μm), with numerous pores and micro-cracks concentrated at grain boundaries and triple junctions. Heterogeneities in porosity, BSE greyscale, and EMPA elemental compositions of the precipitated albite at the reaction front suggest multiple nucleation events from repeated fluid influx. Based on the combined microstructural and geochemical observations, the interplay between cataclasis and interface-coupled reactions appears to have localized weakening and bolstered fracture propagation through the host rock. Cataclasis-generated fracture networks that facilitated fluid infiltration, and ensuing fluid-mediated reactions further weakened the rock. These findings demonstrate the impact of fluid-rock interactions on rupture conditions and fault zone evolution, informing models of slip behavior and the mechanical weakening of fault zones in hydrated systems.

References

Altherr, R., Kreuzer, H., Wendt, I., Lenz, H., Wagner, G. A., Keller, J., Harre, W., & Höhndorf, A. (1982). A Late Oligocene/Early Miocene high temperature belt in the Attic-Cycladic crystalline complex (SE Pelagonian, Greece). *Geologisches Jahrbuch*, 23, 97-164.

Andriessen, P. A. M., Boelrijk, N. A. I. M., Hebeda, E. H., Priem, H. N. A., Verdurnen, E. A. Th., & Verschure, R. H. (1979). Dating the events of metamorphism and granitic magmatism in the Alpine orogen of Naxos (Cyclades, Greece). *Contributions to Mineralogy and Petrology*, 69(3), 215-225. https://doi.org/10.1007/BF00372323

Andriessen, P. A. M., Banga, G., & Hebeda, E. H. (1987). Isotopic age study of pre-Alpine rocks in the basal units on Naxos, Sikinos and Ios, Greek Cyclades. *Geologic en Mijnbouw*, 66(3), 3-14.

Avigad, D., & Garfunkel, Z. (1989). Low-angle faults above and below a blueschist belt—Tinos Island, Cyclades, Greece. *Terra Nova*, 1(2), 182-187. https://doi.org/10.1111/J.1365-3121.1989.TB00350.X

Bachmann, F., Hielscher, R., & Schaeben, H. (2010). Texture analysis with MTEX- Free and open-source software toolbox. *Solid State Phenomena*, 160, 63-68. https://doi.org/10.4028/www.scientific.net/SSP.160.63

Bakowsky, C., Schneider, D. A., Grasemann, B., Dubosq, R., & Ducharme, T. (2025) Crustal architecture and low-temperature geochronology of a Cycladic tectonic window on NE Attica Peninsula, Greece. *Tectonics,* in press.

Barras, F., & Brantut, N. (2025). Shear localisation controls the dynamics of earthquakes. *Nature Communications,* 16(1), 711. https://doi.org/10.1038/s41467-024-55363-y

Barth, N. C., Boulton, C., Carpenter, B. M., Batt, G. E., & Toy, V. G. (2013). Slip localization on the southern Alpine Fault, New Zealand. *Tectonics*, 32(3), 620-640. https://doi.org/10.1002/TECT.20041

Barth, N. C., Hacker, B. R., Seward, G. G. E., Walsh, E. O., Young, D., & Johnston, S. (2010). Strain within the ultrahigh-pressure Western Gneiss region of Norway recorded by quartz CPOs. *Geological Society Special Publication*, 335, 663-685. https://doi.org/10.1144/sp335.27

Bessiere, E., Rabillard, A., Précigout, J., Arbaret, L., Jolivet, L., Augier, R., Menant, A., & Mansard, N. (2018). Strain localization within a syntectonic intrusion in a back-arc extensional context: The Naxos monzogranite (Greece). *Tectonics*, 37(2), 558-587. https://doi.org/10.1002/2017TC004801

Bestmann, M., Pennacchioni, G., Nielsen, S., Göken, M., & de Wall, H. (2012). Deformation and ultrafine dynamic recrystallization of quartz in pseudotachylyte-bearing brittle faults: A matter of

a few seconds. *Journal of Structural Geology*, 38, 21-38. https://doi.org/10.1016/J.JSG.2011.10.001

Bestmann, M., Pennacchioni, G., Mostefaoui, S., Göken, M., & de Wall, H. (2016). Instantaneous healing of micro-fractures during coseismic slip: Evidence from microstructure and Ti in quartz geochemistry within an exhumed pseudotachylyte-bearing fault in tonalite. *Lithos*, 254-255, 84-93. https://doi.org/10.1016/J.LITHOS.2016.03.011

Blacic, J. D., & Christie, J. M. (1984). Plasticity and hydrolytic weakening of quartz single crystals. *Journal of Geophysical Research: Solid Earth*, 89(B6), 4223-4239. https://doi.org/10.1029/JB089IB06P04223

Blake, J. C., Bonneau, M., Geyssant, J., Kienast, J. R., Lepvrier, C., Maluski, H., & Papanikolaou, D. (1981). A geologic reconnaissance of the Cycladic blueschist belt, Greece. *GSA Bulletin*, 92(5), 247-254. https://doi.org/10.1130/0016-7606(1981)92<247:AGROTC>2.0.CO;2

Bolhar, R., Ring, U., & Allen, C. M. (2010). An integrated zircon geochronological and geochemical investigation into the Miocene plutonic evolution of the Cyclades, Aegean Sea, Greece: Part 1: Geochronology. *Contributions to Mineralogy and Petrology*, 160, 719-742. https://doi.org/10.1007/s00410-010-0504-4

Bons, P. D., & Jessell, M. W. (1999). Micro-shear zones in experimentally deformed octachloropropane. *Journal of Structural Geology*, 21(3), 323-334. https://doi.org/10.1016/S0191-8141(98)90116-X

Bos, B., & Spiers, C. J. (2002). Fluid-assisted healing processes in gouge-bearing faults: Insights from experiments on a rock analogue system. *Pure and Applied Geophysics*, 159(11-12), 2537-2566. https://doi.org/10.1007/S00024-002-8747-2

Brantut, N., Schubnel, A., Rouzaud, J. N., Brunet, F., & Shimamoto, T. (2008). High-velocity frictional properties of a clay-bearing fault gouge and implications for earthquake mechanics. *Journal of Geophysical Research: Solid Earth*, 113(10), B10401. https://doi.org/10.1029/2007JB005551

Brichau, S., Ring, U., Ketcham, R. A., Carter, A., Stockli, D., & Brunel, M. (2006). Constraining the long-term evolution of the slip rate for a major extensional fault system in the central Aegean, Greece, using thermochronology. *Earth and Planetary Science Letters*, 241(1-2), 293-306. https://doi.org/10.1016/J.EPSL.2005.09.065

Brun, J. P., & Faccenna, C. (2008). Exhumation of high-pressure rocks driven by slab rollback. *Earth and Planetary Science Letters*, 272(1-2), 1-7. https://doi.org/10.1016/j.epsl.2008.02.038

Buick, I. S. (1991). Mylonite fabric development on Naxos, Greece. *Journal of Structural Geology*, 13(6), 643-655. https://doi.org/10.1016/0191-8141(91)90027-G

Buick, I. S., & Holland, T. J. B. (1989). The P-T-t path associated with crustal extension, Naxos, Cyclades, Greece. *Geological Society Special Publication*, 43, 365-369. https://doi.org/10.1144/GSL.SP.1989.043.01.3

Cao, S., Neubauer, F., Bernroider, M., & Liu, J. (2013). The lateral boundary of a metamorphic core complex: The Moutsounas shear zone on Naxos, Cyclades, Greece. *Journal of Structural Geology*, 54, 103-128. https://doi.org/10.1016/j.jsg.2013.07.002

Cao, S., Neubauer, F., Bernroider, M., Genser, J., Liu, J., & Friedl, G. (2017). Low-grade retrogression of a high-temperature metamorphic core complex: Naxos, Cyclades, Greece. *Bulletin of the Geological Society of America*, 129(1-2), 93-117. https://doi.org/10.1130/B31502.1

Cervellon, A., Hémery, S., Kürnsteiner, P., Gault, B., Kontis, P., & Cormier, J. (2020). Crack initiation mechanisms during very high cycle fatigue of Ni-based single crystal superalloys at high temperature. *Acta Materialia*, 188, 131-144. https://doi.org/10.1016/J.ACTAMAT.2020.02.012

Chester, F. M., & Chester, J. S. (1998). Ultracataclasite structure and friction processes of the Punchbowl fault, San Andreas system, California. *Tectonophysics*, 295(1-2), 199-221. https://doi.org/10.1016/S0040-1951(98)00121-8

Chester, J. S., Chester, F. M., & Kronenberg, A. K. (2005). Fracture surface energy of the Punchbowl fault, San Andreas system. *Nature*, 437(7055), 133-136. https://doi.org/10.1038/nature03942

Conrad, E. M., Tisato, N., Carpenter, B. M., & Di Toro, G. (2023). Influence of frictional melt on the seismic cycle: insights from experiments on rock analog material. *Journal of Geophysical Research: Solid Earth*, 128(1), e2022JB025695. https://doi.org/10.1029/2022JB025695

Corwin, E. I., Jaeger, H. M., & Nagel, S. R. (2005). Structural signature of jamming in granular media. *Nature*, 435(7045), 1075-1078. https://doi.org/10.1038/NATURE03698

Cowie, P. A., & Shipton, Z. K. (1998). Fault tip displacement gradients and process zone dimensions. *Journal of Structural Geology*, 20(8), 983-997. https://doi.org/10.1016/S0191-8141(98)00029-7

Crameri, F. (2018). Scientific colour-maps. *Zenodo*, https://doi.org/10.5281/zenodo.1243862

Di Toro, G., Hirose, T., Nielsen, S., Pennacchioni, G., & Shimamoto, T. (2006). Natural and experimental evidence of melt lubrication of faults during earthquakes. Science, 311(5761), 647-649. https://doi.org/10.1126/science.1121012.

Dubosq, R., Camacho, A., Rogowitz, A., Zhang, S., & Gault, B. (2024). Influence of high-strain deformation on major element mobility in garnet: Nanoscale evidence from atom probe

tomography. *Journal of Metamorphic Geology*, 42(3), 355-372. https://doi.org/10.1111/JMG.12758

Ducharme, T. A., Schneider, D. A., Grasemann, B., & Klonowska, I. (2022). Stretched thin: Oligocene extrusion and ductile thinning of the Basal Unit along the Evia Shear Zone, NW Cyclades, Greece. *Tectonics*, 41(12), e2022TC007561. https://doi.org/10.1029/2022TC007561

Duchêne, S., Aïssa, R., & Vanderhaeghe, O. (2006). Pressure-temperature-time evolution of metamorphic rocks from Naxos (Cyclades, Greece): constraints from thermobarometry and Rb/Sr dating. *Geodinamica Acta*, 19(5), 301-321. https://doi.org/10.3166/ga.19.301-321

Dürr, S., Altherr, R., Keller, J., Okrusch, M., & Seidel, E. (1978). The median Aegean crystalline belt: stratigraphy, structure, metamorphism, magmatism. *In* Cloos, H., Roeder, D., & Schmidt, K., eds., *Alps, Apennines, Hellenides:* Schweizerbart, Stuttgart, 38, 455-476.

Feenstra, A. (1985). Metamorphism of bauxites on Naxos, Greece [Ph.D. thesis], *Geologica Ultraiectina*, 39, 1-206.

Feenstra, A., & Wunder, B. (2002). Dehydration of diasporite to corundite in nature and experiment. *Geology*, 30(2), 119-122. https://doi.org/10.1130/0091-7613(2002)030<0119:DODTCI>2.0.CO;2

Fitz Gerald, J. D., Boland, J. N., McLaren, A. C., Ord, A., & Hobbs, B. E. (1991). Microstructures in water-weakened single crystals of quartz. *Journal of Geophysical Research*, 96(B2), 2139-2155. https://doi.org/10.1029/90JB02190

Fitz Gerald, J. D., & Stünitz, H. (1993). Deformation of granitoids at low metamorphic grade. I: Reactions and grain size reduction. *Tectonophysics*, 221(3-4), 269-297. https://doi.org/10.1016/0040-1951(93)90163-E

Gautier, P., Brun, J.-P, & Jolivet, L. (1993). Structure and kinematics of Upper Cenozoic extensional detachment on Naxos and Paros (Cyclades Islands, Greece). *Tectonics*, 12(5), 1180-1194. https://doi.org/10.1029/93TC01131

Goscombe, B. D., & Passchier, C. W. (2003b). Asymmetric boudins as shear sense indicators - an assessment from field data. *Journal of Structural Geology*, 25(4), 575-589. https://doi.org/10.1016/S0191-8141(02)00045-7

Grasemann, B., Schneider, D. A., Stöckli, D. F., & Iglseder, C. (2012). Miocene bivergent crustal extension in the Aegean: Evidence from the western Cyclades (Greece). *Lithosphere*, 4(1), 23-39. https://doi.org/10.1130/L164.1

Halfpenny, A., Prior, D. J., & Wheeler, J. (2006). Analysis of dynamic recrystallization and nucleation in a quartzite mylonite. *Tectonophysic*s, 427(1-4), 3-14. https://doi.org/10.1016/J.TECTO.2006.05.016

Heermance, R., Shipton, Z. K., & Evans, J. P. (2003). Fault structure control on fault slip and ground motion during the 1999 rupture of the Chelungpu Fault, Taiwan. *Bulletin of the Seismological Society of America*, 93(3), 1034-1050. https://doi.org/10.1785/0120010230

Hejl, E., Riedl, H., & Weingartner, H. (2002). Post-plutonic unroofing and morphogenesis of the Attic-Cycladic complex (Aegean, Greece). *Tectonophysics*, 349(1-4), 37-56. https://doi.org/10.1016/S0040-1951(02)00045-8

Henjes-Kunst, F., Altherr, R., Kreuzer, H., & Hansen, B. T. (1988). Disturbed U-Th-Pb systematics of young zircons and uranothorites: the case of the Miocene Aegean granitoids (Greece). *Chemical Geology: Isotope Geoscience Section*, 73(2), 125-145. https://doi.org/10.1016/0168-9622(88)90011-5

Hentschel, F., Trepmann, C. A., & Janots, E. (2019). Deformation of feldspar at greenschist facies conditions-the record of mylonitic pegmatites from the Pfunderer Mountains, Eastern Alps. *Solid Earth*, 10(1), 95-116. https://doi.org/10.5194/SE-10-95-2019

Hielscher, R., Bartel, F., & Britton, B. (2019). Gazing at crystal balls: electron backscatter diffraction pattern analysis and cross correlation on the sphere. *Ultramicroscopy*, 207, 112836. https://doi.org/10.1016/j.ultramic.2019.112836

Hobbs, B. E. (1968). Recrystallization of single crystals of quartz. *Tectonophysics*, 6(5), 353-401. https://doi.org/10.1016/0040-1951(68)90056-5

Hodge, M., Fagereng, Biggs, J., & Mdala, H. (2018). Controls on early-rift geometry: New perspectives from the Bilila-Mtakataka Fault, Malawi. *Geophysical Research Letters*, 45(9), 3896-3905. https://doi.org/10.1029/2018GL077343

Holland, T., & Blundy, J. (1994). Non-ideal interactions in calcic amphiboles and their bearing on amphibole-plagioclase thermometry. *Contributions to Mineralogy and Petrology*, 116(4), 433-447. https://doi.org/10.1007/BF00310910

Hövelmann, J., Putnis, A., Geisler, T., Schmidt, B. C., & Golla-Schindler, U. (2010). The replacement of plagioclase feldspars by albite: Observations from hydrothermal experiments. *Contributions to Mineralogy and Petrology*, 159(1), 43-59. https://doi.org/10.1007/S00410-009-0415-4

Huet, B., Labrousse, L., & Jolivet, L. (2009). Thrust or detachment? Exhumation processes in the Aegean: Insight from a field study on Ios (Cyclades, Greece). *Tectonics*, 28(3), TC3007. https://doi.org/10.1029/2008TC002397

Jansen, J. B. H. (1973). The geology of Greece, Island of Naxos, scale 1/50,000. Institute of Geology and Mineral Exploration, Athens.

Jansen, J. B. H. (1977). Metamorphism on Naxos, Greece [Ph.D. thesis]. Utrecht University, Utrecht, 110 p.

Jansen, J. B. H., & Schuiling, R. D. (1976). Metamorphism on Naxos; petrology and geothermal gradients. *American Journal of Science*, 276(10), 1225-1253. https://doi.org/10.2475/AJS.276.10.1225

Jolivet, L., & Brun, J. P. (2010). Cenozoic geodynamic evolution of the Aegean. *International Journal of Earth Sciences*, 99(1), 109-138. https://doi.org/10.1007/s00531-008-0366-4

Jolivet, L., Rimmelé, G., Oberhänsli, R., Goffé, B., & Candan, O. (2004). Correlation of syn-orogenic tectonic and metamorphic events in the Cyclades, the Lycian nappes and the Menderes massif. Geodynamic implications. *Bulletin de La Société Géologique de France*, 175(3), 217-238. https://doi.org/10.2113/175.3.217

Jolivet, L., Lecomte, E., Huet, B., Denèle, Y., Lacombe, O., Labrousse, L., Le Pourhiet, L., & Mehl, C. (2010). The North Cycladic Detachment System. *Earth and Planetary Science Letters*, 289(1-2), 87-104. https://doi.org/10.1016/J.EPSL.2009.10.032

John, B. E., & Howard, K. A. (1995). Rapid extension recorded by cooling-age patterns and brittle deformation, Naxos, Greece. *Journal of Geophysical Research*, 100(B6), 9969-9979. https://doi.org/10.1029/95JB00665

Katzir, Y., Garfunkel, Z., Avigad, D., & Matthews, A. (2007). The geodynamic evolution of the Alpine orogen in the Cyclades (Aegean Sea, Greece): insights from diverse origins and modes of emplacement of ultramafic rocks. *Geological Society Special Publication*, 291, 17-40. https://doi.org/10.1144/SP291.2

Keay, S., Lister, G., & Buick, I. (2001). The timing of partial melting, Barrovian metamorphism and granite intrusion in the Naxos metamorphic core complex, Cyclades, Aegean Sea, Greece. *Tectonophysics*, 342(3-4), 275-312. https://doi.org/10.1016/S0040-1951(01)00168-8

Kirkpatrick, J. D., & Rowe, C. D. (2013). Disappearing ink: How pseudotachylytes are lost from the rock record. *Journal of Structural Geology*, 52(1), 183-198. https://doi.org/10.1016/J.JSG.2013.03.003

Kirkpatrick, J. D., & Shipton, Z. K. (2009). Geologic evidence for multiple slip weakening mechanisms during seismic slip in crystalline rock. *Journal of Geophysical Research: Solid Earth*, 114(B12), 12401. https://doi.org/10.1029/2008JB006037

Labotka, T. C., Cole, D. R., Fayek, M., Riciputi, L. R., & Stadermann, F. J. (2004). Coupled cation and oxygen-isotope exchange between alkali feldspar and aqueous chloride solution. *American Mineralogist*, 89(11-12), 1822-1825. https://doi.org/10.2138/AM-2004-11-1229

Lanari, P., Vidal, O., De Andrade, V., Dubacq, B., Lewin, E., Grosch, E. G., & Schwartz, S. (2014). XMapTools: A MATLAB©-based program for electron microprobe X-ray image processing and geothermobarometry. *Computers and Geosciences*, 62, 227-240. https://doi.org/10.1016/j.cageo.2013.08.010

Lamont, T. N., Searle, M. P., Waters, D. J., Roberts, N. M. W., Palin, R. M., Smye, A., et al. (2020). Compressional origin of the Naxos metamorphic core complex, Greece: structure, petrography, and thermobarometry. *GSA Bulletin*, 132(1-2), 149-197. https://doi.org/10.1130/B31978.1

Lenthe, W. C., Singh, S., & Graef, M. De. (2019). A spherical harmonic transform approach to the indexing of electron back-scattered diffraction patterns. *Ultramicroscopy*, 207, 112841. https://doi.org/10.1016/J.ULTRAMIC.2019.112841

Lin, A. (1994). Glassy pseudotachylyte veins from the Fuyun fault zone, northwest China. *Journal of Structural Geology*, 16(1), 71-83. https://doi.org/10.1016/0191-8141(94)90019-1

Lin, A. (1996). Injection veins of crushing-originated pseudotachylyte and fault gouge formed during seismic faulting. *Engineering Geology*, 43(2-3), 213-224. https://doi.org/10.1016/0013-7952(96)00062-2

Lin, A. (2019). Thermal pressurization and fluidization of pulverized cataclastic rocks formed in seismogenic fault zones. *Journal of Structural Geology*, 125, 278-284. https://doi.org/10.1016/j.jsg.2017.12.010

Lin, A., Yamashita, K., & Tanaka, M. (2013). Repeated seismic slips recorded in ultracataclastic veins along active faults of the Arima-Takatsuki Tectonic Line, southwest Japan. *Journal of Structural Geology*, 48, 3-13. https://doi.org/10.1016/J.JSG.2013.01.005

Lister, G. S., Banga, G., & Feenstra, A. (1984). Metamorphic core complexes of Cordilleran type in the Cyclades, Aegean Sea, Greece. *Geology*, 12(4), 221-225. https://doi.org/10.1130/0091-7613(1984)12<221:MCCOCT>2.0.CO;2

Lloyd, G. E., & Knipe, R. J. (1992). Deformation mechanisms accommodating faulting of quartzite under upper crustal conditions. *Journal of Structural Geology*, 14(2), 127-143. https://doi.org/10.1016/0191-8141(92)90052-X

Mair, K., & Marone, C. (1999). Friction of simulated fault gouge for a wide range of velocities and normal stresses. *Journal of Geophysical Research: Solid Earth*, 104(B12), 28899-28914. https://doi.org/10.1029/1999JB900279

Mancktelow, N., Zwingmann, H., & Mulch, A. (2016). Timing and conditions of clay fault gouge formation on the Naxos detachment (Cyclades, Greece). *Tectonics*, 35(10), 2334-2344. https://doi.org/10.1002/2016TC004251

Mancktelow, N. S., Camacho, A., & Pennacchioni, G. (2022). Time-lapse record of an earthquake in the dry felsic lower continental crust preserved in a pseudotachylyte-bearing fault. *Journal of Geophysical Research: Solid Earth*, 127(4). https://doi.org/10.1029/2021JB022878

McKay, L., Lunn, R. J., Shipton, Z. K., Pytharouli, S., & Roberts, J. J. (2021). Do intraplate and plate boundary fault systems evolve in a similar way with repeated slip events? *Earth and Planetary Science Letters*, 559, 116757. https://doi.org/10.1016/J.EPSL.2021.116757

McLaren, A. C., & Pryer, L. L. (2001). Microstructural investigation of the interaction and interdependence of cataclastic and plastic mechanisms in feldspar crystals deformed in the semi-brittle field. *Tectonophysics*, 335(1-2), 1-15. https://doi.org/10.1016/S0040-1951(01)00042-7

Menegon, L., Pennacchioni, G., Malaspina, N., Harris, K., & Wood, E. (2017). Earthquakes as precursors of ductile shear zones in the dry and strong lower crust. *Geochemistry, Geophysics, Geosystems,* 18(12), 4356-4374. https://doi.org/10.1002/2017GC007189

Michalchuk, S. P., Zertani, S., Renard, F., Fusseis, F., Chogani, A., Plümper, O., & Menegon, L. (2023). Dynamic evolution of porosity in lower-crustal faults during the earthquake cycle. *Journal of Geophysical Research: Solid Earth*, 128(8), e2023JB026809. https://doi.org/10.1029/2023JB026809

Moreira, N., & Dias, R. (2018). Domino structures evolution in strike-slip shear zones; the importance of the cataclastic flow. *Journal of Structural Geology*, 110, 187-201. https://doi.org/10.1016/J.JSG.2018.01.010

Neumann, B. (2000). Texture development of recrystallised quartz polycrystals unraveled by orientation and misorientation characteristics. *Journal of Structural Geology*, 22(11-12), 1695-1711. https://doi.org/10.1016/S0191-8141(00)00060-2

Norberg, N., Neusser, G., Wirth, R., & Harlov, D. (2011). Microstructural evolution during experimental albitization of K-rich alkali feldspar. *Contributions to Mineralogy and Petrology*, 162(3), 531-546. https://doi.org/10.1007/s00410-011-0610-y

Onasch, C. M., Farver, J. R., & Dunne, W. M. (2010). The role of dilation and cementation in the formation of cataclasite in low temperature deformation of well cemented quartz-rich rocks. *Journal of Structural Geology*, 32(12), 1912-1922. https://doi.org/10.1016/j.jsg.2010.04.013

Peillod, A., Ring, U., Glodny, J., & Skelton, A. (2017). An Eocene/Oligocene blueschist-greenschist facies P-T loop from the Cycladic Blueschist Unit on Naxos Island, Greece: Deformation-related re-equilibration vs. thermal relaxation. *Journal of Metamorphic Geology*, 35(7), 805-830. https://doi.org/10.1111/jmg.12256

Pennacchioni, G., Di Toro, G., Brack, P., Menegon, L., & Villa, I. M. (2006). Brittle-ductile-brittle deformation during cooling of tonalite (Adamello, Southern Italian Alps). *Tectonophysics*, 427(1-4), 171-197. https://doi.org/10.1016/J.TECTO.2006.05.019

Pe-Piper, G. (2000). Origin of S-type granites coeval with I-type granites in the Hellenic subduction system, Miocene of Naxos, Greece. *European Journal of Mineralogy*, 12(4), 859-875. https://doi.org/10.1127/0935-1221/2000/0012-0859

Pe-Piper, G., Kotopouli, C. N., & Piper, D. J. W. (1997). Granitoid rocks of Naxos, Greece: regional geology and petrology. *Geological Journal*, 32(2), 153-171. https://doi.org/10.1002/(SICI)1099-1034(199706)32:2<153::AID-GJ737>3.0.CO;2-1

Petley-Ragan, A., Dunkel, K. G., Austrheim, H., Ildefonse, B., & Jamtveit, B., (2018). Microstructural records of earthquakes in the lower crust and associated fluid-driven metamorphism in plagioclase-rich granulites. *Journal of Geophysical Research: Solid Earth*, 123(5), 3729-3746. https://doi.org/10.1029/2017JB015348

Philpotts, A. R. (1964). Origin of pseudotachylites. *American Journal of Science*, 262(8), 1008-1035. https://doi.org/10.2475/AJS.262.8.1008

Pichon, X. Le, & Angelier, J. (1979). The Hellenic arc and trench system: A key to the neotectonic evolution of the eastern Mediterranean area. *Tectonophysics*, 60(1), 1-42. https://doi.org/https://doi.org/10.1016/0040-1951(79)90131-8

Platt, J. D., Brantut, N., & Rice, J. R. (2015). Strain localization driven by thermal decomposition during seismic shear. *Journal of Geophysical Research: Solid Earth*, 120(6), 4405-4433. https://doi.org/10.1002/2014JB011493

Plümper, O., & Putnis, A. (2009). The complex hydrothermal history of granitic rocks: Multiple feldspar replacement reactions under subsolidus conditions. *Journal of Petrology*, 50(5), 967-987. https://doi.org/10.1093/petrology/egp028

Pryer, L. L. (1993). Microstructures in feldspars from a major crustal thrust zone: The Grenville Front, Ontario, Canada. *Journal of Structural Geology*, 15(1), 21-36. https://doi.org/10.1016/0191-8141(93)90076-M

Putnis, A. (2009). Mineral replacement reactions. *In* Oelkers, E. H., & Schott, J., eds., Thermodynamics and Kinetics of Water-Rock Interaction, *Reviews in Mineralogy and Geochemistry*, 70 (1), 87-124. https://doi.org/10.2138/rmg.2009.70.3

Putnis, A., & Austrheim, H. (2010). Fluid-induced processes: Metasomatism and metamorphism. *Geofluids*, 10(1-2), 254-269. https://doi.org/10.1111/j.1468-8123.2010.00285.x

Rice, J. R. (2006). Heating and weakening of faults during earthquake slip. *Journal of Geophysical Research: Solid Earth*, 111(B5). https://doi.org/10.1029/2005JB004006

Rogowitz, A., Zaefferer, S., & Dubosq, R. (2018). Direct observation of dislocation nucleation in pyrite using combined electron channelling contrast imaging and electron backscatter diffraction. *Terra Nova*, 30(6), 423-430. https://doi.org/10.1111/TER.12358

Rowe, C. D., & Griffith, W. A. (2015). Do faults preserve a record of seismic slip: A second opinion. *Journal of Structural Geology*, 78, 1-26. https://doi.org/10.1016/j.jsg.2015.06.006

Rowe, C. D., Moore, J. C., Meneghini, F., & McKeirnan, A. W. (2005). Large-scale pseudotachylytes and fluidized cataclasites from an ancient subduction thrust fault. *Geology*, 33(12), 937-940. https://doi.org/10.1130/G21856.1

Schmid, S. M., & Casey, M. (1986). Complete fabric analysis of some commonly observed quartz c-axis patterns. *In* Hobbs, B. E., & Heard, H. C., eds., Mineral and Rock Deformation: Laboratory Studies, *American Geophysical Union Geophysical Monograph Series,* 36, 263-286. https://doi.org/10.1029/GM036p0263

Scholz, C. H. (2019). The mechanics of earthquakes and faulting, 3rd ed. *Cambridge University Press*, Cambridge. https://doi.org/10.1017/9781316681473

Segall, P., & Pollard, D. P. (1983). Nucleation and growth of strike slip faults in granite. *Journal of Geophysical Research: Solid Earth*, 88(B1), 555-568. https://doi.org/10.1029/JB088IB01P00555

Seward, D., Vanderhaeghe, O., Siebenaller, L., Thomson, S., Hibsch, C., Zingg, A., Holzner, P., Ring, U., & Duchêne, S. (2009). Cenozoic tectonic evolution of Naxos Island through a multi-faceted approach of fission-track analysis. *Geological Society Special Publication*, 321, 179-196. https://doi.org/10.1144/sp321.9

Shipton, Z. K., Soden, A. M., Kirkpatrick, J. D., Bright, A. M., & Lunn, R. J. (2006). How thick is a fault? Fault displacement-thickness scaling revisited. *In* Abercrombie, R., McGarr, A., Di Toro, G., & Kanamori, H., eds., Earthquakes: Radiated Energy and the Physics of Faulting, *American Geophysical Union Geophysical Monograph Series*, 170, 193-198. https://doi.org/https://doi.org/10.1029/170GM19

Sibson, R. H. (1973). Interactions between temperature and pore-fluid pressure during earthquake faulting and a mechanism for partial or total stress relief. *Nature Physical Science* 243, 66-68. https://doi.org/10.1038/physci243066a0

Sibson, R. H. (1975). Generation of pseudotachylyte by ancient seismic faulting. *Geophysical Journal of the Royal Astronomical Society*, 43(3), 775-794. https://doi.org/10.1111/J.1365-246X.1975.TB06195.X

Sibson, R. H. (1977). Fault rocks and fault mechanisms. *Journal of the Geological Society*, 133(3), 191-213. https://doi.org/10.1144/GSJGS.133.3.0191

Siebenaller, L., Boiron, M. C., Vanderhaeghe, O., Hibsch, C., Jessell, M. W., Andre-Mayer, A. S., France-Lanord, C., & Photiades, A. (2013). Fluid record of rock exhumation across the brittle-ductile transition during formation of a metamorphic core complex (Naxos Island, Cyclades, Greece). *Journal of Metamorphic Geology*, 31(3), 313-338. https://doi.org/10.1111/jmg.12023

Soret, M., Précigout, J., Stünitz, H., Raimbourg, H., Plümper, O., Osselin, F., Lee, A., & Rividi, L. (2025). Deep crustal deformation driven by reaction-induced weakening. *Nature Communications*, 16(1), 1-14. https://doi.org/10.1038/s41467-025-60692-7

Spray, J. G. (1995). Pseudotachylyte controversy: Fact or friction? *Geology*, 23(12), 1119-1122. https://doi.org/10.1130/0091-7613(1995)023<1119:PCFOF>2.3.CO;2

Stipp, M., Stünitz, H., Heilbronner, R., & Schmid, S. M. (2002). The eastern Tonale fault zone: a 'natural laboratory' for crystal plastic deformation of quartz over a temperature range from 250 to 700°C. *Journal of Structural Geology*, 24(12), 1861-1884. https://doi.org/10.1016/S0191-8141(02)00035-4

Stünitz, H. (1998). Syndeformational recrystallization - dynamic or compositionally induced? *Contributions to Mineralogy and Petrology*, 131(2), 219-236. https://doi.org/10.1007/S004100050390

Stünitz, H., & Fitz Gerald, J. D. (1993). Deformation of granitoids at low metamorphic grade. II: Granular flow in albite-rich mylonites. *Tectonophysics*, 221(3-4), 299-324. https://doi.org/10.1016/0040-1951(93)90164-F

Swanson, M. T. (1992). Fault structure, wear mechanisms and rupture processes in pseudotachylyte generation. *Tectonophysics*, 204(3-4), 223-242. https://doi.org/10.1016/0040-1951(92)90309-T

Tullis, J., & Yund, R. A. (1987). Transition from cataclastic flow to dislocation creep of feldspar: Mechanisms and microstructures. *Geology*, 15(7), 606-609. https://doi.org/10.1130/0091-7613(1987)15<606:TFCFTD>2.0.CO;2

Tullis, J., & Yund, R. A. (1992). The brittle-ductile transition in feldspar aggregates: an experimental study. *In* Evans, B., & Wong, T., eds., International Geophysics, *Academic Press,* 51, 89-117. https://doi.org/https://doi.org/10.1016/S0074-6142(08)62816-8

Ujiie, K., Yamaguchi, A., Kimura, G., & Toh, S. (2007a). Fluidization of granular material in a subduction thrust at seismogenic depths. *Earth and Planetary Science Letters*, 259(3-4), 307-318. https://doi.org/10.1016/J.EPSL.2007.04.049

Ujiie, K., Yamaguchi, H., Sakaguchi, A., & Toh, S. (2007b). Pseudotachylytes in an ancient accretionary complex and implications for melt lubrication during subduction zone earthquakes. *Journal of Structural Geology*, 29(4), 599-613. https://doi.org/10.1016/J.JSG.2006.10.012

Urai, J. L., Schuiling, R. D., & Jansen, J. B. H. (1990). Alpine deformation on Naxos (Greece). *Geological Society Special Publication*, 54, 509-522. https://doi.org/10.1144/GSL.SP.1990.054.01.47

Vanderhaeghe, O., Kruckenberg, S. C., Gerbault, M., Martin, L., Duchêne, S., & Deloule, E. (2018). Crustal-scale convection and diapiric upwelling of a partially molten orogenic root (Naxos dome, Greece). *Tectonophysics*, 746, 459-469. https://doi.org/10.1016/J.TECTO.2018.03.007

Vanderhaeghe, O. (2004). Structural development of the Naxos migmatite dome, *in* Whitney, D. L., Teyssier, C., & Siddoway, C. S., eds., Gneiss Domes in Orogeny, *Geological Society of America Special Paper*, 380, 211-227. https://doi.org/10.1130/0-8137-2380-9.211

Walters, J. B. (2022). MinPlot: A mineral formula recalculation and plotting program for electron probe microanalysis. *Mineralogia*, 53(1), 52-67. https://doi.org/10.2478/mipo-2022-0005

White, S. H., Burrows, S. E., Carreras, J., Shaw, N. D., & Humphreys, F. J. (1980). On mylonites in ductile shear zones. *Journal of Structural Geology*, 2(1-2), 175-187. https://doi.org/10.1016/0191-8141(80)90048-6

Wijbrans, J. R., & McDougall, I. (1988). Metamorphic evolution of the Attic Cycladic metamorphic belt on Naxos (Cyclades, Greece) utilizing $^{40}Ar/^{39}Ar$ age spectrum measurements. *Journal of Metamorphic Geology*, 6(5), 571-594. https://doi.org/10.1111/J.1525-1314.1988.TB00441.X

Yehya, A., & Rice, J. R. (2020). Influence of fluid-assisted healing on fault permeability structure. *Journal of Geophysical Research: Solid Earth*, 125(10), e2020JB020553. https://doi.org/10.1029/2020JB020553

Zhang, L., Li, H., Sun, Z., Cao, Y., & Wang, H. (2021). Microstructural evolution of pseudotachylyte-bearing rocks during increasing temperatures: evidence from rock-heating experiments. *Journal of Structural Geology*, 149, 104398. https://doi.org/10.1016/J.JSG.2021.104398

Zuo, J., Webb, A. A. G., Piazolo, S., Wang, Q., Müller, T., Ramírez-Salazar, A., & Haproff, P. J. (2021). Tectonics of the Isua Supracrustal Belt 2: microstructures reveal distributed strain in the absence of major fault structures. *Tectonics*, 40(3), e2020TC006514. https://doi.org/10.1029/2020TC006514

Appendix A. Supplementary material

Table S1. EBSD map acquisition parameters

sample	instrument	working distance	voltage	current	binning	step size
N23-02 Bp Scan 4	Zeiss Merlin 1	15.1 mm	20 kV	7.0 nA	8x8	1.25 μm
N23-02 Bp Scan 6	Zeiss Merlin 1	15.0 mm	20kV	7.0 nA	8x8	2.5 μm
N23-02 Cll2 Montage	Zeiss Merlin 2	15.8 mm	30 kV	7.0 nA	8x8	1.5 μm
N23-02 Dp Scan 3	Zeiss Merlin 1	16.7 mm	20 kV	7.0 nA	8x8	1.25 μm

Table S2. EMPA mineral chemistry

sample	phase	spot # †	SiO_2	Al_2O_3	FeO	MnO	MgO	CaO	Na_2O	K_2O	BaO	Xan	Xab	Xor
CII2 2	orthoclase	1	30.61	10.13	0.03	0.00	0.02	0.02	0.30	13.86	0.45	0.00	0.03	0.97
CII2 2	orthoclase	2	30.35	10.11	0.02	0.00	0.00	0.01	0.30	13.53	0.26	0.00	0.03	0.97
CII2 2	orthoclase	3	30.17	9.87	0.02	0.00	0.00	0.00	0.95	12.44	0.15	0.00	0.10	0.90
CII2 2	orthoclase	4	30.29	10.01	0.03	0.00	0.01	0.02	1.22	12.14	0.66	0.00	0.13	0.87
CII2 2	orthoclase	5	30.89	10.42	0.02	0.00	0.00	0.02	1.11	12.48	0.21	0.00	0.12	0.88
Cll2 2	orthoclase	6	30.48	10.09	0.01	0.00	0.00	0.02	0.30	14.05	0.31	0.00	0.03	0.97
Cll2 2	orthoclase	7	30.16	10.21	0.02	0.00	0.01	0.03	0.40	13.74	0.53	0.00	0.04	0.96
Cll2 2	orthoclase	8	30.03	10.13	0.05	0.00	0.01	0.03	0.55	13.27	0.58	0.00	0.06	0.94
Cll2 2	medium grey albite	1	29.06	13.04	0.01	0.00	0.03	3.94	6.56	0.24	0.06	0.24	0.74	0.02
Cll2 2	medium grey albite	2	29.07	12.48	0.30	0.00	0.09	3.28	6.66	0.27	0.03	0.21	0.77	0.02
Cll2 2	medium grey albite	3	28.38	13.30	0.02	0.00	0.00	4.40	6.32	0.07	0.05	0.28	0.72	0.00
Cll2 2	medium grey albite	4	28.78	13.48	0.06	0.00	0.00	4.34	6.17	0.18	0.06	0.28	0.71	0.01
Cll2 2	medium grey albite	5	28.65	13.23	0.00	0.00	0.00	4.37	6.38	0.13	0.03	0.27	0.72	0.01
CII2 2	dark grey albite	1	42.20	3.97	0.11	0.00	0.02	0.93	1.46	0.08	0.02	0.25	0.72	0.03
CII2 2	dark grey albite	2	43.14	2.25	0.00	0.00	0.00	0.80	0.62	0.09	0.02	0.39	0.56	0.05
CII2 2	dark grey albite	3	44.28	0.71	0.03	0.00	0.00	0.11	0.28	0.02	0.05	0.17	0.79	0.04
CII2 2	dark grey albite	4	41.53	3.49	0.03	0.00	0.01	0.63	1.53	0.41	0.05	0.16	0.71	0.12
CII2 2	albite rim	1	33.24	10.98	0.05	0.00	0.01	3.07	5.24	0.09	0.04	0.24	0.75	0.01
CII2 2	albite rim	2	32.01	11.31	0.01	0.00	0.04	1.47	5.96	0.52	0.04	0.11	0.84	0.05

† see Figure 9 for spot locations

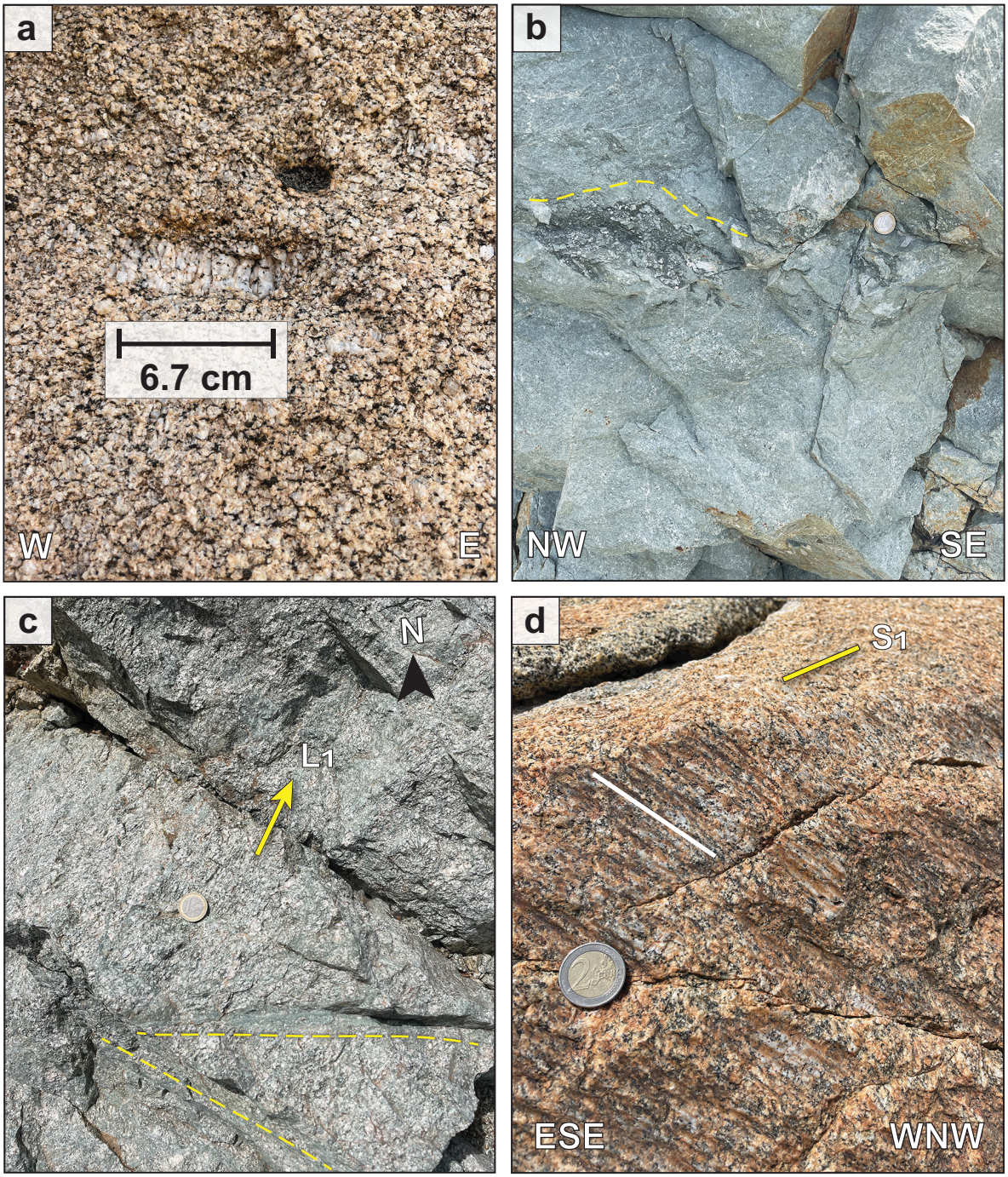

Figure S1. Representative field photos of the Naxos granodiorite and deformation structures. (**a**) Undeformed granodiorite from zone 0 (Bessiere et al., 2018), with elongated potassium feldspar phenocrysts (353637 E, 4103387 N). (**b**) Cataclastic zone immediately below the NPDS at Cape Achapsi. Few discrete lenses and veinlets of ultracataclasite (darker material, highlighted as yellow dashed lines) are preserved in the brittle overprint. Green tinge of the rock is from extensive chloritization (358649 E, 4110321 N). (**c**) Granodiorite outcrop photo at Galini, with a stretching lineation (L1) of 11°-037°. Ultracataclastic veins (highlighted as yellow dashed lines) are visible in the chloritized granodiorite (360003 E, 4109438 N). (**d**) Striations (white line; 29°-330°) along an exposed fault plane at Stelida (353684 E, 4105857 N). 1€ coin for scale in (b-c): 23 mm diameter, 2€ coin for scale in (d): 26 mm diameter.

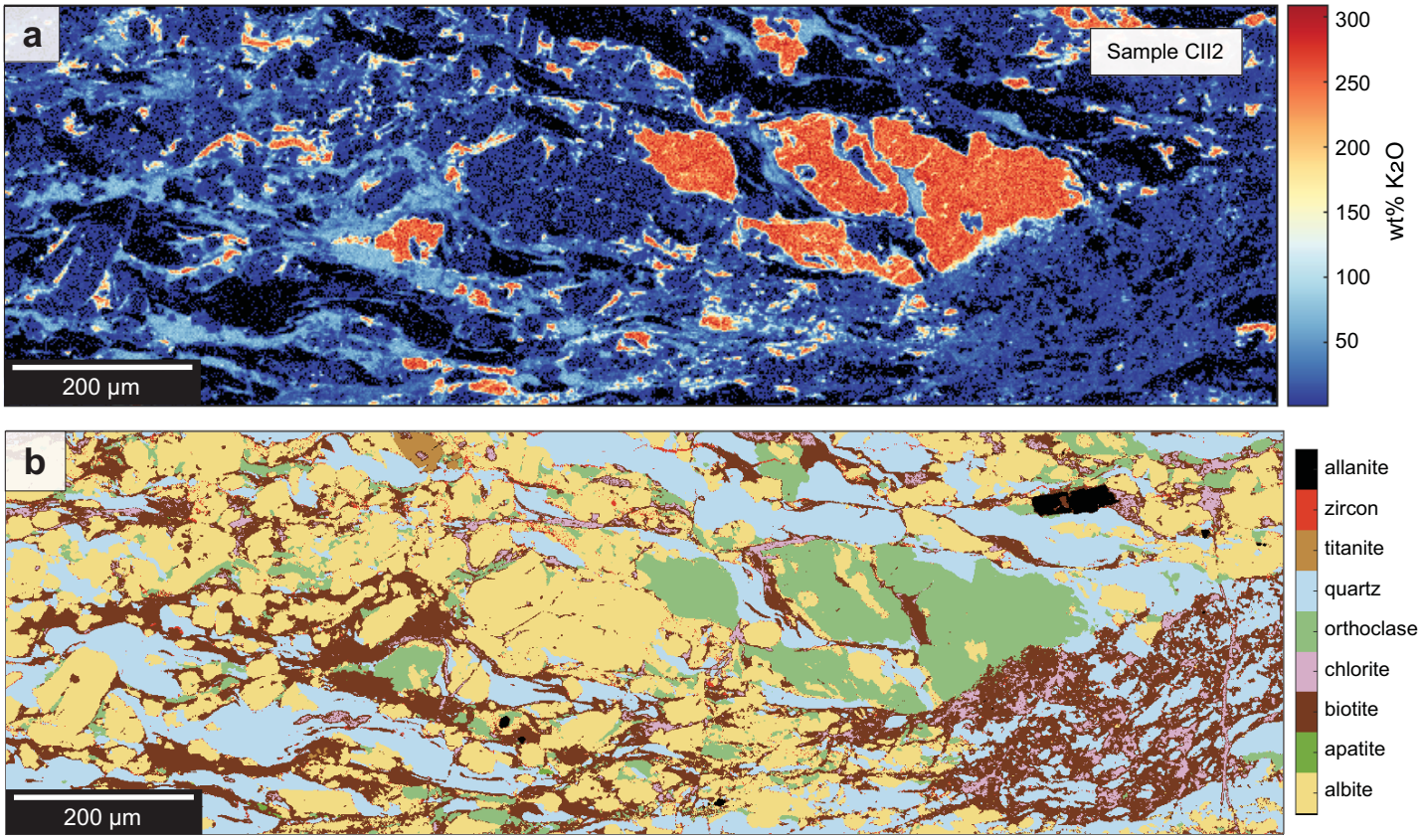

Figure S2. (**a**) Micro-XRF potassium (wt% K_2O) distribution map for sample Cll2. (**b**) Corresponding mineral phase plot of sample Cll2.

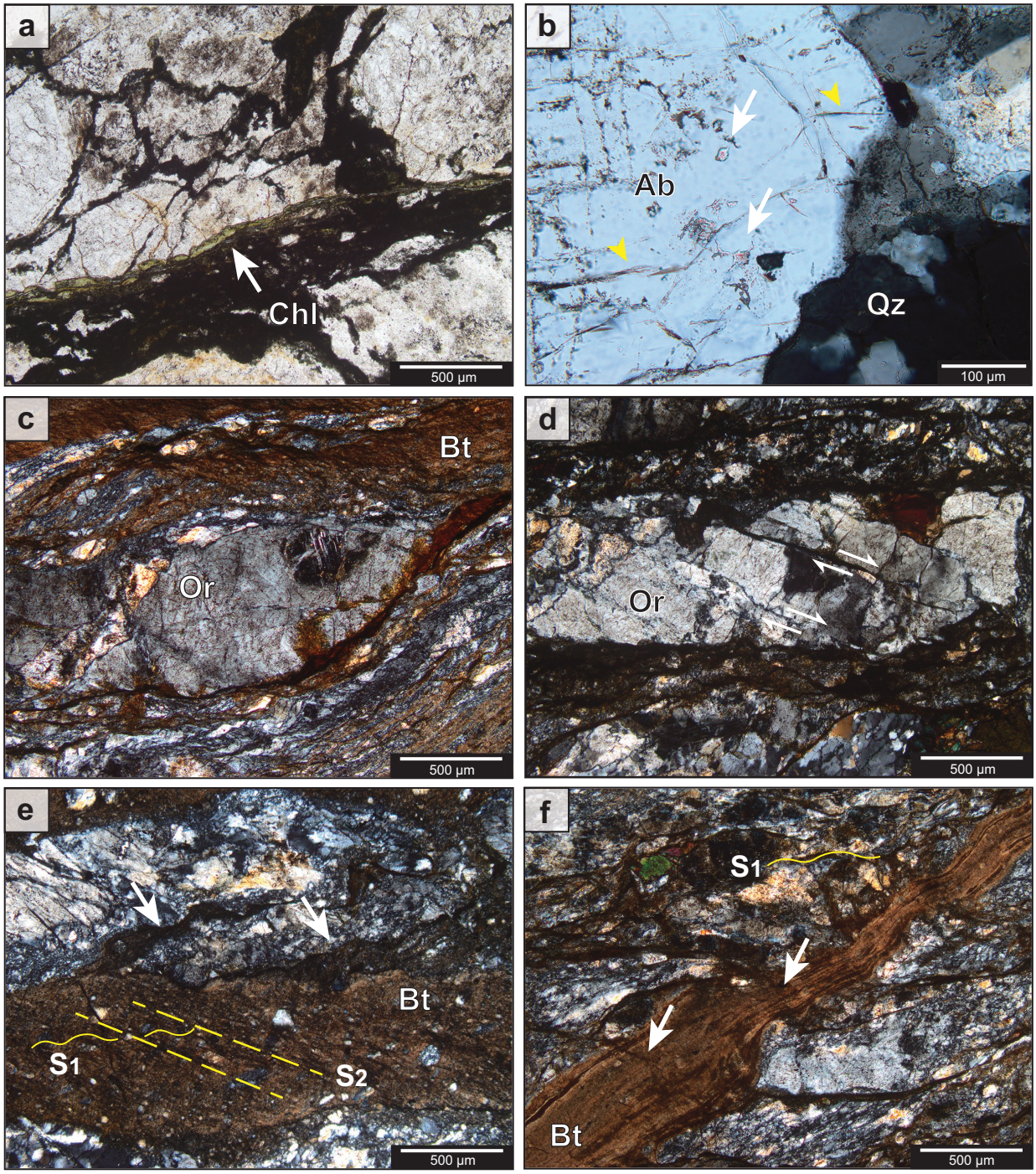
a
Chl
500 µm
b
Ab
Qz
100 µm
c
Bt
Or
500 µm
d
Or
500 µm
e
Bt
S1
S2
500 µm
f
S1
Bt
500 µm

Figure S3. Cross and plane polarized light photomicrographs of microstructures in the granodiorite matrix and ultracataclastic veins. Albite: Ab, orthoclase: Or, biotite: Bt, chlorite: Chl. All thin sections are oriented parallel to lineation. (**a**) PPL image of a dark pseudotachylytic vein lined with chlorite along the vein margin (353763 E, 4105947 N). (**b**) Fluid inclusions (white arrows) and fractures (yellow arrows) within an albite phenocryst in the low strain granodiorite. (353637 E, 4103387 N). (**c**) Sigmoid orthoclase porphyroclast in the high strain granodiorite, surrounded by biotite-rich ultracataclastic veins and a foliated fine-grained matrix with elongated and sigmoidal albite, orthoclase and quartz grains (353681 E, 4105900 N). (**d**) Bookshelf micro-fracturing of an orthoclase clast in sample Cll2, the relative shear sense is marked by half arrows (353649 E, 4105948 N). (**e**) Biotite-rich ultracataclastic vein parallel to foliation (S_1) with a dark rim and crenulated off-shoot veinlets (white arrows). Subrounded porphyroclast fragments (up to 70 μm) are preserved in the vein. A recurrent, evenly spaced planar feature in the vein material is suggestive of a crenulation cleavage (S_2) (353681 E, 4105900 N). (**f**) Biotite-rich ultracataclastic vein, steeper than foliation (S_1), overprinted by several foliation parallel veinlets which are indicated by white arrows (353651 E, 4105925 N).

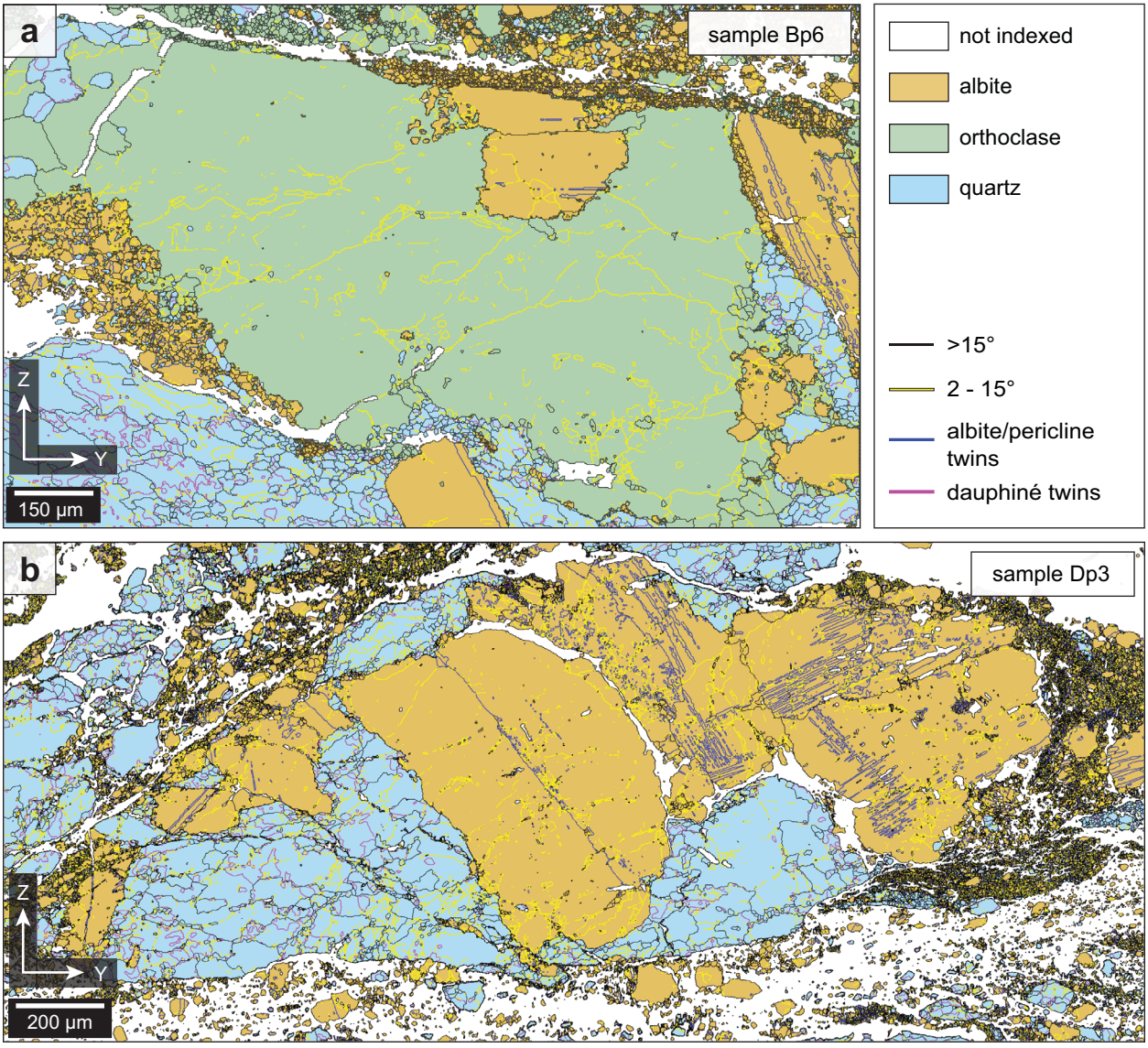

Figure S4. Electron backscatter diffraction (EBSD) phase and grain boundary maps of albite, orthoclase and quartz microstructures proximal to ultracataclastic veins. Both samples cut perpendicular to lineation, the y (horizontal) axis is subparallel to foliation. Points are colored by phase with low angle grain boundaries (LAGBs) outlined in yellow, twins in albite outlined in blue, and dauphiné twins in quartz outlined in magenta. (**a**) Orthoclase porphyroclast along a vein margin (top) in sample Bp6. (**b**) Relict albite porphyroclasts in a quartz and albite matrix in sample Dp3. LAGBs increase towards clast rims and ultracataclastic vein margins (bottom and top of map).

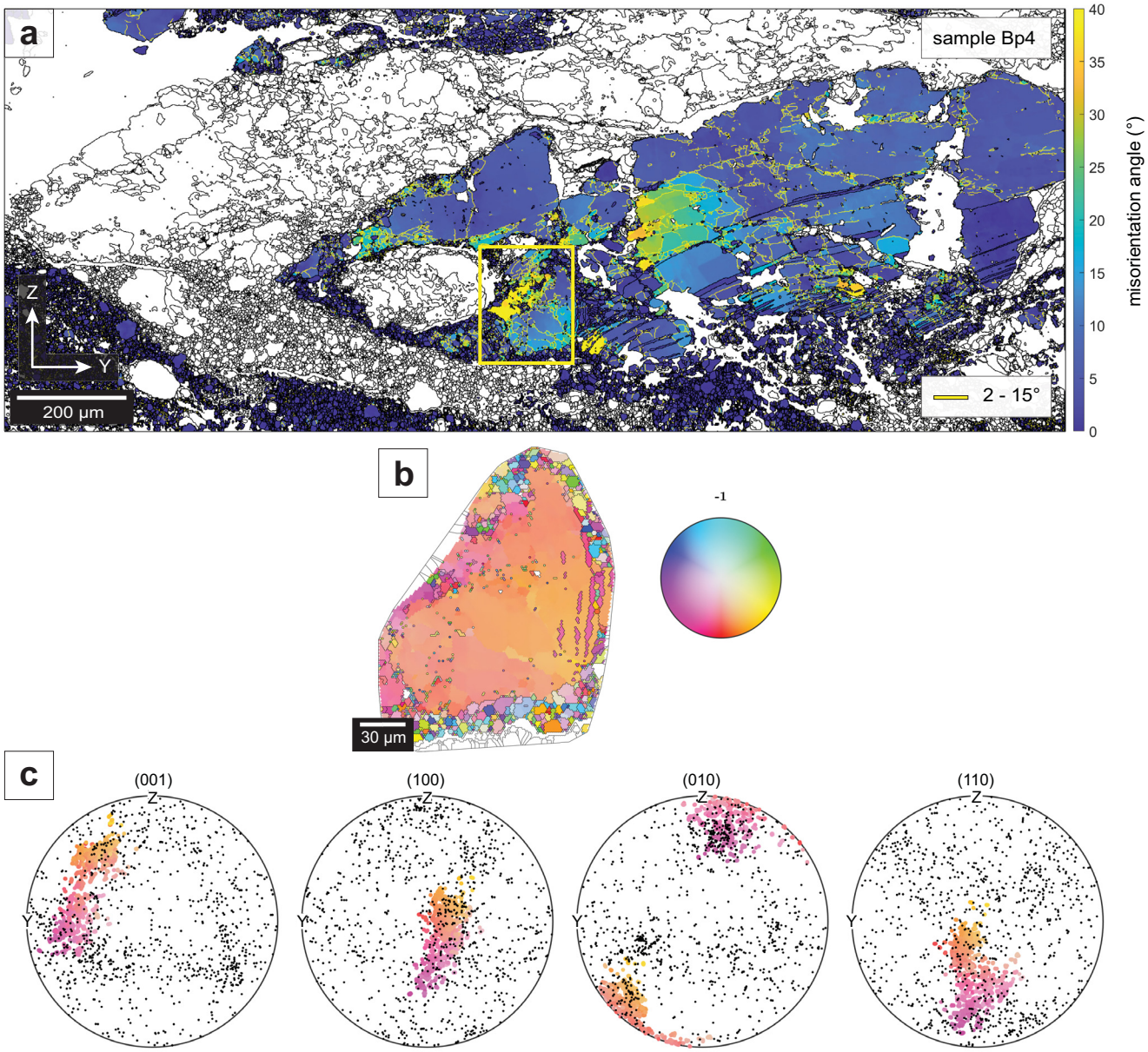

Figure S5. Grain orientation analysis on albite populations in sample Bp4. (**a**) Orientation deviation angle map of albite showing misorientation relative to grain average orientation, and LAGBs outlined in yellow. The map displays a continuous to heterogeneous misorientation pattern in the host rock, with a maximum misorientation angle of ~73°. Fine grains of albite (<50 µm) occur at the clast rims and vein tip, with maximum misorientations of ~10°. The pole figure subset area in (b-c) is outlined in red. (**b**) IPF-Z map of albite grains in the analysis subset and corresponding IPF key for albite. (**c**) Lower hemisphere pole figure showing the IPF-Z orientation spread of pixels in the large albite host clast (120 µm), shown relative to the mean orientation of the small albite grains (<30 µm) surrounding the clast (black markers, one point per grain).

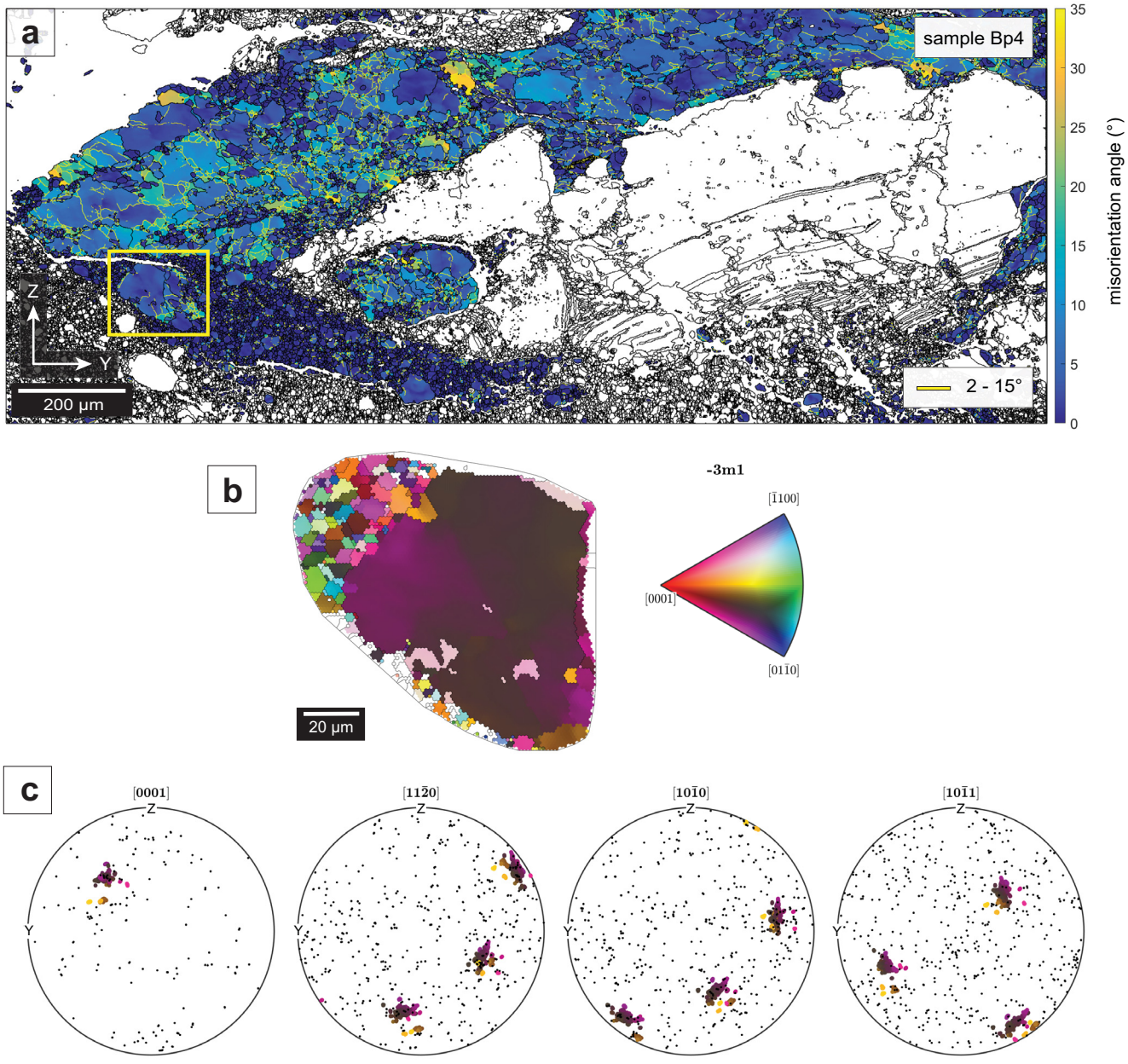

Figure S6. Grain orientation analysis on quartz populations in sample Bp4. (**a**) Orientation deviation angle map of quartz showing misorientation relative to grain average orientation, and LAGBs outlined in yellow. Quartz displays a continuous misorientation pattern with a maximum misorientation angle of ~46° in the host rock. Misorientation increases towards the vein, in which fine quartz grains have very low (~0-8°) misorientations. Pole figure subset in (b-c) is outlined in red. (**b**) IPF-Z map of quartz grains in the analysis subset and corresponding IPF key for quartz. (**c**) Lower hemisphere pole figure showing the IPF-Z orientation spread of a larger quartz clast (86 µm), shown relative to the mean orientation of the small quartz grains (<40 µm) surrounding the clast (black markers, one point per grain).

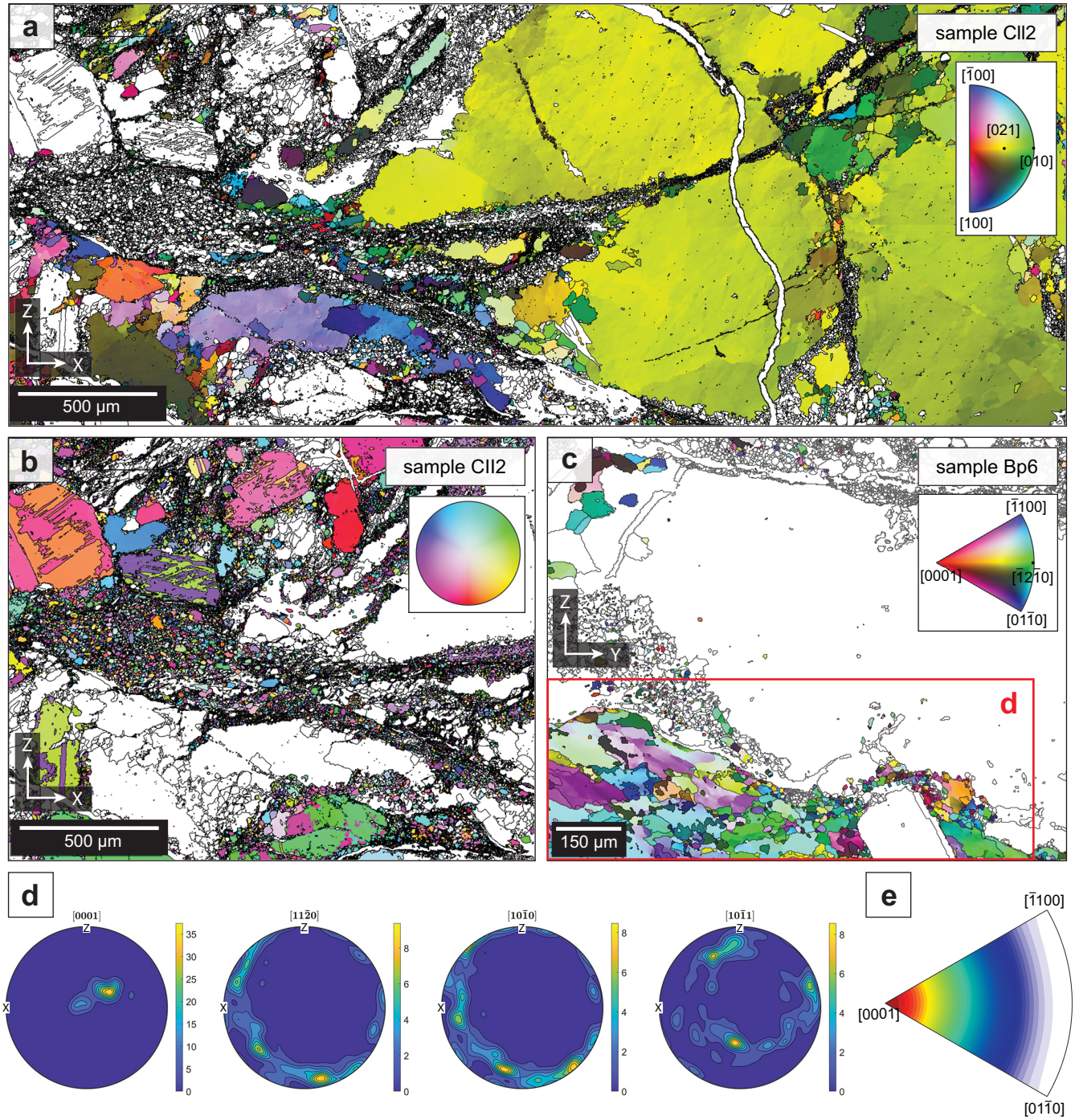

Figure S7. (**a**) Inverse pole figure (IPF) map showing orthoclase grain orientations colored with respect to the y-direction in sample Cll2 (the y-direction is orthogonal to the thin section plane). (**b**) IPF-Y map of albite grains in sample Cll2. The albite fragments in the ultracataclastic vein are randomly oriented, with no crystallographic relationship to the surrounding albite clasts. (**c**) IPF-Z map of quartz grains in sample Bp6 showing elongated grains in the bottom left with the c-axis {0001} oriented perpendicular to the z-direction. Red box shows the grains plotted in the quartz pole figure in (d). (**d**) Lower hemisphere pole figure showing the crystallographic-preferred orientation of quartz (grains >20 µm), with a maximum near to [Y] in the c-axis. (**e**) Distribution of misorientation axes of the quartz grains plotted on the pole figure. The axes concentrate around the [c] axis, corresponding to dominant prism-<a> dislocation slip.

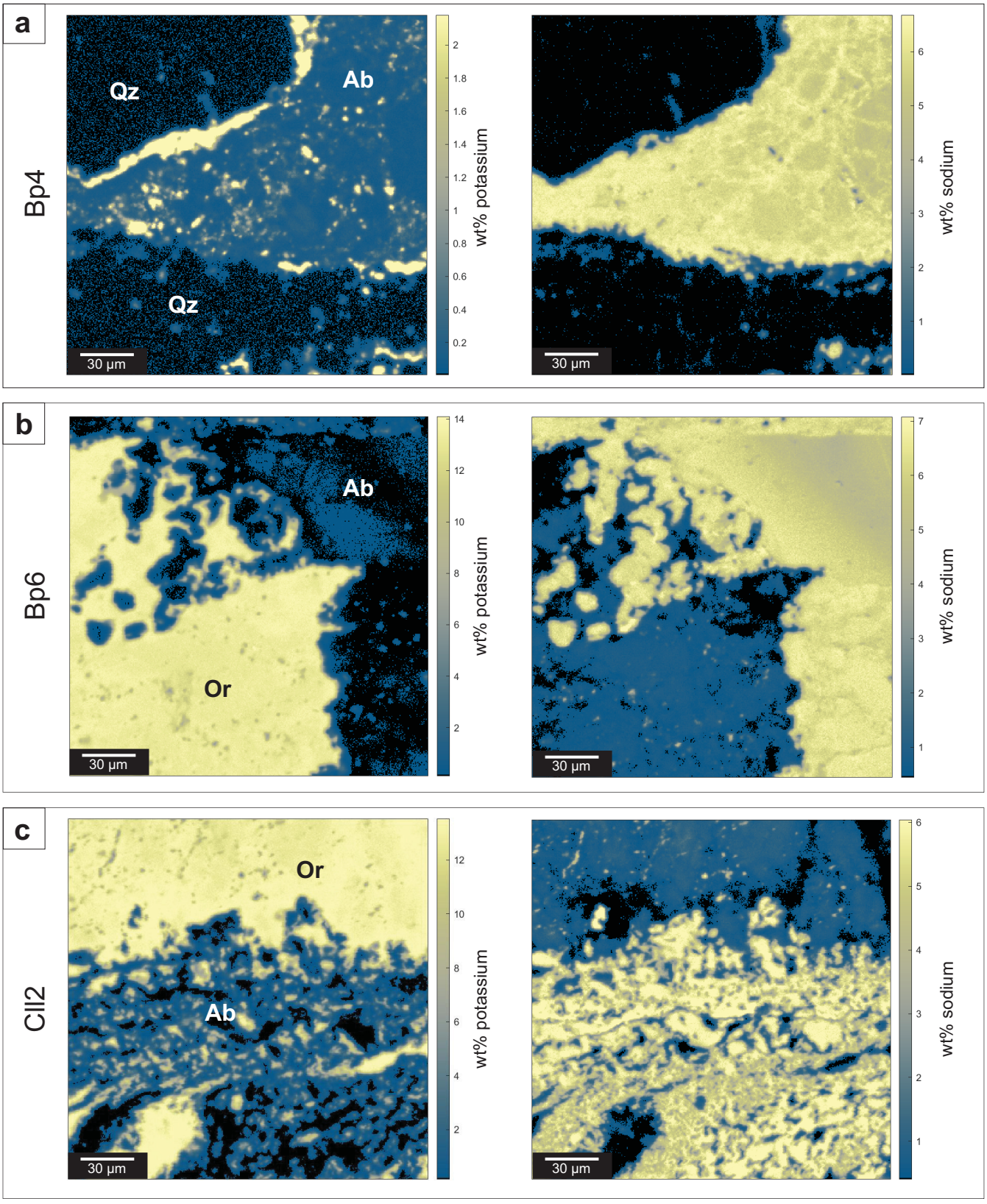

Figure S8. (**a-c**) Additional EMPA X-ray maps for potassium and sodium in sample Bp4, Bp6 and Cll2 display local compositional variations within the feldspar clasts. Orthoclase porphyroclasts exhibit potassium-depleted rims, while the albite aggregates show regions of sodium depletion, particularly at phase boundaries.

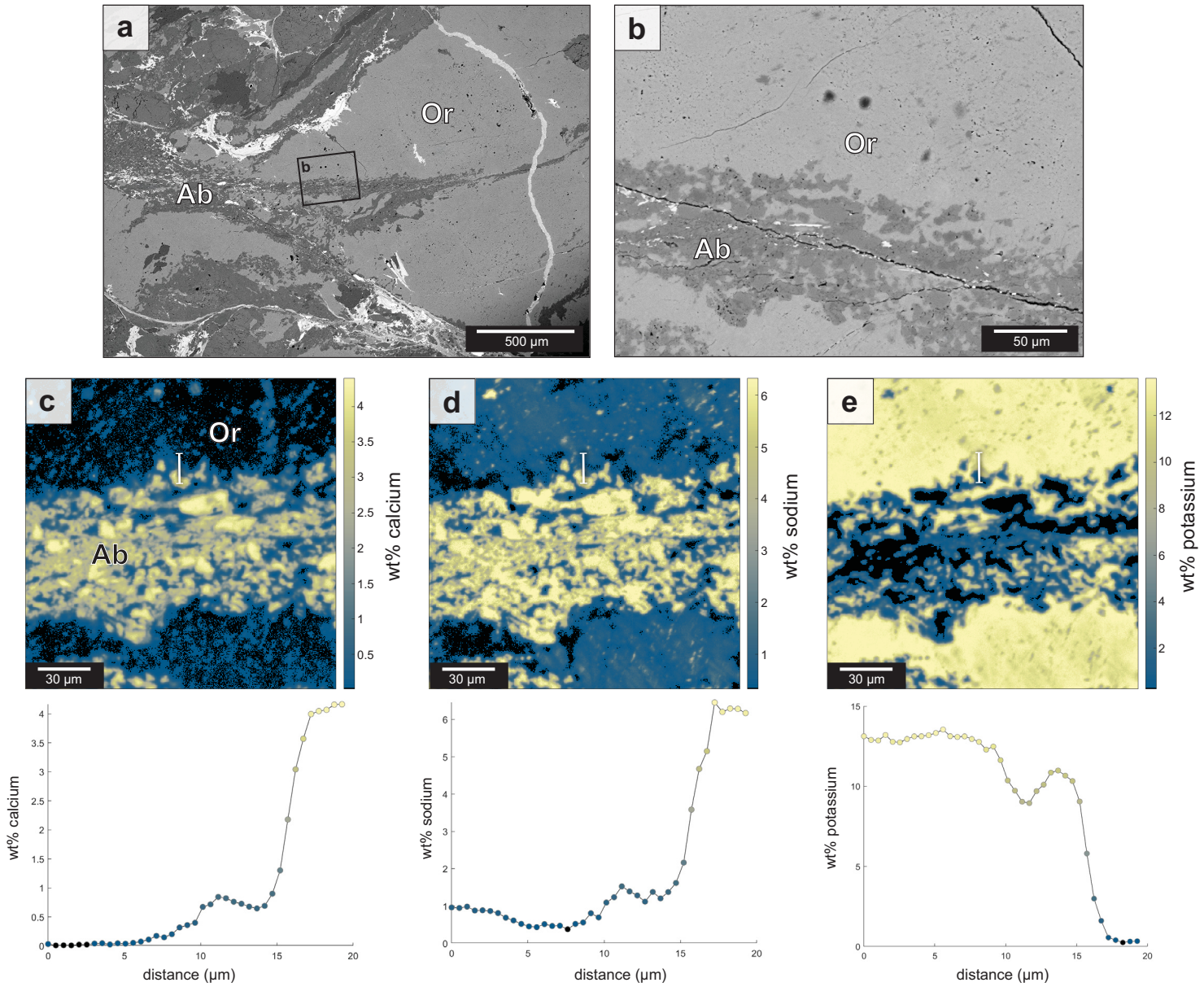

Figure S9. (a-b) BSE images of sample Cll2, the black box in (a) outlines the BSE image area of (b) and the EMPA mapped region. (**c-e**) EMPA X-ray maps for Ca, Na and K in sample Cll2 displaying compositional variations along orthoclase and albite porphyroclast rims at the edge of an ultracataclastic vein margin. The orthoclase porphyroclast shows a cuspate interface with the fine-grained albite aggregates (<45 µm) lining the vein. Orthoclase rims are depleted in K, while albite rims are depleted in Ca and Na. Below, the associated graphs show the change in wt% of each element across the phase boundary. The sampled transect is marked by a white line on the X-ray maps.